Nonlinear Dyn (2023) 111:2183–2202
https://doi.org/10.1007/s11071-022-07928-z

ORIGINAL PAPER

An electro-mechanical dynamic model for flexoelectric energy harvesters

Tran Quoc Thai · Xiaoying Zhuang · Timon Rabczuk

Received: 5 May 2022 / Accepted: 6 September 2022 / Published online: 11 October 2022

Abstract Flexoelectricity is a universal electro-mechanical coupling effect that occurs in dielectrics of all symmetric groups and becomes dominant at the micro- and nano-scales. It plays an important role in evaluating micro-electro-mechanical systems (MEMS) such as energy harvesters which convert vibrational energy to electric energy. At finer length scales, micro-inertia effects significantly contribute to the behavior of flexoelectric materials due to the mechanical dispersion. Hence, to properly characterize the vibrational behavior of MEMS, a reliable theoretical approach is required accounting for all possible phenomena that affect the output of the system such as voltage or power density. In this work, we present a consistent (dynamic) model and associated computational framework for flexoelectric structures to study the characteristics of the vibrational behavior of energy harvesters showing the dominance of the flexoelectric effect at micro- and nano-scales. In this context, we quantify the impact of the micro-inertia length scale and the flexoelectric dynamic parameter on both frequency and time responses of energy harvesters.

Keywords Strain gradient elasticity/couple stress theory · Micro inertial effect · Cubic Perovskite · Dynamic flexoelectric effect · Large rotation/geometric nonlinearity · Size dependent piezoelectricity/flexoelectricity · Energy harvesting

1 Introduction

Experimental evidence and observations on thin metal films and wires [1–4], micro-epoxy beams [5,6], and CFRP composites [7] have indicated significant size-dependent phenomena which become dominant at micro- and nanoscopic levels. In continuum mechanics, this effect is commonly modeled by enriching the conventional continuum theories with some material length scale parameter(s). This in turn has lead to the development of higher-order gradient theories such as the couple stress-based elasticity theory proposed by Mindlin and Tiersten [8], Toupin [9] and Koiter [10]; strain gradient elasticity theory based on the seminal work of Mindlin [11], Eringen and Suhubi [12], Green and Rivlin [13], Kröner [14], Mindlin and Eshel [15] and Germain [16], surface stress elasticity theory developed by Mindlin [17], the surface energy model from Gurtin and Murdoch [18,19] and integral nonlocal theories proposed by Eringen [20]. As these theories pro-

X. Zhuang
Department of Geotechnical Engineering, College of Civil Engineering, Tongji University, Shanghai 200092, China

T. Q. Thai · X. Zhuang (✉)
Chair of Computational Science and Simulation Technology, Institute of Photonics, Department of Mathematics and Physics, Leibniz University Hannover, Appelstr. 11, 30167 Hannover, Germany
e-mail: zhuang@iop.uni-hannover.de

T. Rabczuk (✉)
Institute of Structural Mechanics, Bauhaus University of Weimar, 99423 Weimar, Germany
e-mail: timon.rabczuk@uni-weimar.de

vide reasonable explanations and their results agreed well with experimental data accounting for size and surface energy effects, they have been applied successfully for characterizing the mechanical behavior of micro- and nano-scale structures.

Micro-electro-mechanical systems (MEMS) have wide applications in many areas including the automotive industry, smart wearable devices, sports equipment and energy harvesters. Capturing the electro-mechanical coupling effect at lower length scales requires an appropriate extension of the strain gradient theories. In classic continuum mechanics, the piezoelectric effect describes the linear relation between the induced electric polarization and the applied mechanical strain. Piezoelectricity exists only in non-centrosymmetric dielectrics. Evidence of 'size-dependent piezoelectricity' was confirmed by Multani and Palkar [21] when they found that decreasing grain sizes of PZT decreases the piezoelectric factor. Other experimental observations of size-dependent piezoelectric have been reported from Mishima et al. [22], Buhlmann et al. [23], Cross [24], Harden et al. [25], Baskaran et al. [26], Catalan et al. [27]. This size dependence is commonly named flexoelectricity [24] and is due to the linear coupling between the electric polarization and strain gradients. Different from piezoelectricity which requires non-centrosymmetric constraint, flexoelectricity is a universal phenomenon that exists in all dielectrics including centrosymmetric materials. Flexoelectricity has a wide range of applications including nanodevices [28,29], sensors and actuators [29–31] and energy harvesters [32–35]. An energy harvester is a self-power autonomous electronic device operated by cultivating available existing power from the surrounding environment such as human movements, solar energy, and wind energy. Similar to conventional piezoelectric energy harvesters, flexoelectric-based energy harvesters convert mechanical energy into electrical energy via the mechanical vibrations of actuators.

While there are numerous contributions about piezoelectric energy harvesters, see Raj et al. [36], Caetano et al. [37], and references therein, there are comparatively few studies on flexoelectricity though they have increased in recent years. Deng et al. [32] proposed a flexoelectric Euler–Bernoulli model to analyze the frequency response functions of energy harvesters. The same method was applied by Faroughi et al. [33] to study the influence of tapering geometric properties on the voltage/power outcomes. A nonlinear flexoelectric beam model for energy harvesters was developed by Wang et al. [35] quantifying the influence of different material parameters such as the gradient index. The material volume ratio coefficient on the generated voltage output of functionally graded flexoelectric energy harvesters was studied by Chu et al. [38]. Majdoub et al. [39] reported that a 5 nm $BaTiO_3$ beam can sustain almost five times the inhomogeneous strain compared to a corresponding macro beam. Deng et al. [32] showed that decreasing the thickness of a flexoelectric beam made of polyvinylidene fluoride (PVDF) from $3\,\mu$m to 0.3 μm leads to a two order increase in the magnitude of the energy conversion efficiency; a similar observation was reported from Wang et al. [35] for nonlinear vibrations of PVDF and from Moura et al. for strontium titanate [40].

Polymer-based piezo- and flexoelectric materials such as PVDF and fiber-reinforced polymers improve the structural bending abilities and therefore promise a higher elastic energy. Flexoelectric beam models have been widely used due to their computational efficiency and simplicity. However, these beam models overestimate the natural frequency. Furthermore, most beam models neglect dynamic contributions. Models, that includes both internal length scale and internal inertia gradient affects, are called dynamically consistent [41–43]. The micro-inertia effect are important to describe dispersive wave propagations [43]. For dielectric materials, considering a crystal made of at least two different atoms and under mechanical accelerated motion, the unit cell is distorted, which leads to a polarization wave with an amplitude proportional to the exciting acceleration. This phenomenon is called dynamic flexoelectricity [44–46] which is nonzero for dielectric materials constructed by different ions due to the mass differences. Deng et al. [34] studied this influence on the performance of energy harvesters employing an Euler–Bernoulli beam model and a reduced-order method. However, the micro-inertia effect was neglected. Furthermore, beam formulations and reduced-order approaches unfortunately cannot capture the complex underlying physics. For vibration problems such as energy harvesting, there are two main issues: firstly, up to date there is no reliable model considering all possible physical phenomena that can influence the output such as voltage and power density. And secondly, no model has been developed that accurately

characterize the vibrational behavior of microstructures.

Thus, we formulate a dynamically consistent model for micro-scale piezo-flexoelectric model by including internal length, internal inertia gradient and flexodynamic effects in the context of nonlinear geometric analysis and develop an IGA (Isogeometric Analysis) formulation to investigate the dynamic/vibrational behaviors of micro-scale energy harvesting structures.

2 Theory of couple stress-based piezo-flexoelectricity

2.1 Energy formulation

The internal energy density of an elastic dielectric can be expressed as [47–49]

$$\psi(\epsilon_{ij}, \epsilon_{ij,k}, P_i) = \frac{1}{2}\epsilon_{ij}\tilde{C}_{ijkl}\epsilon_{kl} + \frac{1}{2}\epsilon_{ij,k}\tilde{H}_{ijklmn}\epsilon_{lm,n} + \frac{1}{2}A_{ij}P_iP_j + \tilde{f}_{ijkl}P_i\epsilon_{jk,l} + \tilde{d}_{ijk}P_i\epsilon_{jk} \quad (1)$$

where $\boldsymbol{\epsilon}$ is the Green–Lagrange strain $\epsilon_{ij} = \frac{1}{2}(F_{ik}F_{jk} - \delta_{ij}) = \frac{1}{2}(u_{i,j} + u_{j,i} + u_{k,i}u_{k,j})$ capturing geometrical nonlinearities, u_i is the displacement vector, P_i the polarization vector, $F_{ij} = \dfrac{\partial x_i}{\partial X_j}$ the deformation gradient, $\tilde{C}_{ijkl}$ the fourth-order elasticity tensor, $\tilde{A}_{ij}$ the dielectric tensor, $\tilde{d}_{ijk}$ the piezoelectric tensor and $\tilde{f}_{ijkl}$ denotes the flexoelectric tensor. For a cubic elastic material tensor, we have $\tilde{C}_{ijkl} = \tilde{C}_{jikl} = \tilde{C}_{ijlk}$, $\tilde{C}_{1111} = C_{11}$, $\tilde{C}_{1122} = C_{22}$ and $\tilde{C}_{2323} = C_{44}$ denoting three independent nonzero components. Taking advantage of Voigt notation, the elasticity tensor C_{ij}, the dielectric tensor A_{ij} and the piezoelectric material d_{ij} can be, respectively, expressed in matrix form as

$$\mathbf{C} = \begin{bmatrix} C_{11} & C_{12} & C_{12} & 0 & 0 & 0 \\ C_{12} & C_{11} & C_{12} & 0 & 0 & 0 \\ C_{12} & C_{11} & C_{12} & 0 & 0 & 0 \\ 0 & 0 & 0 & C_{44} & 0 & 0 \\ 0 & 0 & 0 & 0 & C_{44} & 0 \\ 0 & 0 & 0 & 0 & 0 & C_{44} \end{bmatrix},$$

$$\mathbf{A} = \begin{bmatrix} 1/\alpha_{11} & 0 & 0 \\ 0 & 1/\alpha_{11} & 0 \\ 0 & 0 & 1/\alpha_{33} \end{bmatrix}$$

$$\text{and } \mathbf{d} = \begin{bmatrix} 0 & 0 & 0 & 0 & d_{15} & 0 \\ 0 & 0 & 0 & d_{15} & 0 & 0 \\ d_{31} & d_{31} & d_{33} & 0 & 0 & 0 \end{bmatrix} \quad (2)$$

where α_{ij} is the electric susceptibility. The flexoelectric tensor of a cubic material has three independent parameters and is computed as [50,51].

$$\tilde{f}_{ijkl} = f_{1122}\delta_{jk}\delta_{il} + f_{1212}(\delta_{ij}\delta_{kl} + \delta_{ik}\delta_{jl}) + (f_{1111} - f_{1122} - 2f_{1212})\delta_{ijkl}, \quad (3)$$

where δ_{ij} is the Kronecker–Delta and δ_{ijkl} is the fourth-order identity tensor which equals to 1 when $i = j = k = l = 1$. The theory of couple stress model is based on the idea of replacing the third-order strain gradient $\epsilon_{ij,k}$ by a traceless second-order tensor $\kappa_{ij} = -e_{iab}\epsilon_{ja,b}$ [8,9] and then decomposing it into a symmetric and an antisymmetric part as $\kappa_{ij} = \kappa^s_{ij} + \kappa^a_{ij}$ (see Appendix A for details). Applying this concept, the energy formulation (27) is expressed as

$$\psi(\epsilon_{ij}, \kappa^s_{ij}, \chi_i) = \psi^{int}(\epsilon_{ij}, \kappa^s_{ij}, \chi_i) + \frac{A_{ij}}{2}P_iP_j + 2\tilde{f}P_i\chi_i + d_{ijk}P_i\epsilon_{jk}. \quad (4)$$

The internal elastic energy is

$$\psi^{int}(\epsilon_{ij}, \kappa^s_{ij}, \chi_i) = \frac{1}{2}\epsilon_{ij}\tilde{C}_{ijkl}\epsilon_{kl} + 8g_2\chi_i\chi_i + g_1\kappa^s_{ij}\kappa^s_{ij}. \quad (5)$$

where g_1 and g_2 are two material parameters of the nonlocal elasticity, i.e., $g_1 = l_1^2C_{12}$ and $g_2 = l_2^2C_{12}$ and the flexoelectric energy is

$$\tilde{f}_{ijk}P_i\kappa_{jk} = \tilde{f}_{ijk}P_i(\kappa^a_{jk} + \kappa^s_{jk}) = \tilde{f}_{ijk}P_i\kappa^a_{jk} = 2\tilde{f}P_i\chi_i \quad (6)$$

where $\tilde{f} = \frac{f_{1122} - f_{1212}}{2}$.

2.2 Conservation of energy and weak formulations

According to the energy balance principle for isothermal processes, the rate of change of the internal and kinetic energies are equal to the work done by the body forces, surface tractions, and electric field, i.e.,

$$P^{int} + P^{kin} = P^{ext} \quad (7)$$

with

$$P^{int} = \frac{D}{Dt}\int_\Omega \psi^{int}(\epsilon_{ij}, \kappa^s_{ij}, \chi_i)d\Omega + \frac{D}{Dt}\int_\Omega \left(\frac{A_{ij}}{2}P_iP_j\right.$$

$$+2\tilde{f}P_i\chi_i-\frac{1}{2}\epsilon_0E_iE_i+d_{ijk}P_i\epsilon_{jk}\Big)d\Omega,$$

$$P^{kin}=\frac{D}{Dt}\int_\Omega\frac{1}{2}\rho v_iv_id\Omega+\frac{D}{Dt}\int_\Omega\frac{1}{2}l^2\rho v_{i,j}v_{i,j}d\Omega+\frac{D}{Dt}\int_\Omega\frac{1}{2}\gamma_{ij}\dot{P}_i\dot{P}_jd\Omega+\frac{D}{Dt}\int_\Omega m_{ij}v_i\dot{P}_jd\Omega,$$

$$P^{ext}=\int_\Omega\rho\dot{v}_i\tilde{b}_id\Omega+\int_{\partial\Omega}\dot{v}_i(\tau_i+t_i)d\Gamma+\frac{D}{Dt}\int_\Omega\phi\tilde{\rho}d\Omega+\frac{D}{Dt}\int_\Omega E_iP_id\Omega, \tag{8}$$

where τ_i and t_i indicate the higher-order traction and traction forces, respectively, $\tilde{b}_i$ denotes the body force, v_i is the velocity vector. The inertia gradient is included to captures the elastic wave dispersion as shown in [41–43]. The dynamic flexoelectric effect describes the response of the polarization to the mechanical acceleration m_{ij} [44–46]. The polarization dynamics is also included in the above equation, i.e., the dynamic energy related to the rate of the polarization γ_{ij} [44,46,52]. Finally, it can be shown that the initial boundary value problem reads

$$+\int_\Omega P_i(2\tilde{f}\delta\chi_i+d_{ijk}\delta\epsilon_{jk})d\Omega+\int_\Omega m_{ij}\ddot{P}_i\delta u_jd\Omega=\int_\Omega\tilde{b}_i\delta u_id\Omega+\int_{\partial\Omega}(t_i+\tau_i)\delta u_id\Gamma, \tag{10}$$

where the acceleration is denoted as $\ddot{u}_i=a_i$. Applying the divergence theorem and integral by part on the micro-inertia gives

$$-\int_\Omega l^2\rho a_{i,jj}\delta u_id\Omega=\int_\Omega l^2\rho a_{i,j}\delta u_{i,j}d\Omega-\int_\Omega l^2\rho a_{i,j}\delta u_iN_jd\Omega. \tag{11}$$

From Askes and Aifantis [43], we know that the term on boundary is $-\int_\Omega l^2\rho a_{i,j}\delta u_iN_jd\Omega=0$ and hence $-\int_\Omega l^2\rho a_{i,jj}\delta u_id\Omega=\int_\Omega l^2\rho a_{i,j}\delta u_{i,j}d\Omega$. This acceleration gradient is an additional positive term ensuring a positive kinetic energy density and thus stability [43]. Equation (10) can be rewritten as

$$\int_\Omega\rho a_i\delta u_id\Omega+\int_\Omega l^2\rho a_{i,j}\delta u_{i,j}d\Omega+\int_\Omega\sigma^m_{ij}\delta\epsilon_{ij}d\Omega+\int_\Omega s^a_i\delta\chi_id\Omega+\int_\Omega s^s_{ij}\delta\kappa_{ij}d\Omega$$

$$\begin{cases}\dot{P}_i(A_{ij}P_j+2\tilde{f}\chi_i+d_{ijk}\epsilon_{jk}+\gamma_{ij}P_j+m_{ij}\dot{v}_j-E_i)=0\text{ in }\Omega, & (9a)\\ v_i(m_{ij}\ddot{P}_j-\rho l^2\dot{v}_{i,jj}+\rho\dot{v}_i-\rho b_i-\sigma_{ij,j}+s^s_{ij,j}+s^a_{ij,j})=0\text{ in }\Omega, & (9b)\\ \dfrac{D\psi^{int}}{Dt}+2\tilde{f}P_i\dot{\chi}_i+d_{ijk}P_i\dot{\epsilon}_{jk}=v_{i,j}(\sigma_{ij}-s^s_{ij}-s^a_{ij})\text{ in }\Omega & (9c)\\ (\sigma_{ij}-s^s_{ij}-s^a_{ij})N_j=\tau_i+t_i\text{ on }\Gamma, & (9d)\\ s_{ijk}N_iN_j=0\text{ on }\Gamma_S & (9e)\\ N_jv_{i,j}=u^{**}\text{ on }\Gamma_{u^{**}} & (9f)\\ N_j\dot{v}_{i,j}=v^{**}\text{ on }\Gamma_{v^{**}}. & (9g)\end{cases}$$

From the local strong form, the integral formulation of the weak form can be obtain by replacing v_i from Eq. (9b) by a test function δu_i and integrate over the domain Ω. After integration by parts and using the divergence theorem in Eq. (9b) leads to

$$\int_\Omega\rho a_i\delta u_id\Omega-\int_\Omega l^2\rho a_{i,jj}\delta u_id\Omega+\int_\Omega\sigma^m_{ij}\delta\epsilon_{ij}d\Omega+\int_\Omega s^a_i\delta\chi_id\Omega\int_\Omega s^s_{ij}\delta\kappa_{ij}d\Omega$$

$$+\int_\Omega P_i(2\tilde{f}\delta\chi_i+d_{ijk}\delta\epsilon_{jk})d\Omega+\int_\Omega m_{ij}\ddot{P}_i\delta u_jd\Omega=\int_\Omega\tilde{b}_i\delta u_id\Omega+\int_{\partial\Omega}(t_i+\tau_i)\delta u_id\Gamma. \tag{12}$$

Gauss's law for an isotropic dielectric material and its corresponding boundary conditions are given as

$$\begin{cases} \nabla \cdot \mathbf{D} = \tilde{\rho} \text{ in } \Omega, & \text{(13a)} \\ \phi = \phi^* \text{ on } \Gamma_{\phi^*}, & \text{(13b)} \\ \mathbf{D} \cdot \hat{\mathbf{N}} = D^* \text{ on } \Gamma_{D^*}. & \text{(13c)} \end{cases}$$

The weak formulation of the electrical problem is obtained by multiplying (13b) with a test function $\delta\phi$ yielding

$$\int_\Omega (\nabla \cdot \mathbf{D}) \delta\phi d\Omega = \int_\Omega \tilde{\rho} \delta\phi d\Omega \quad (14)$$

Applying integration by parts

$$-\int_\Omega \mathbf{D} \cdot \nabla(\delta\phi) d\Omega = \int_\Omega \tilde{\rho}\delta\phi d\Omega - \int_{\partial\Omega} \delta\phi \mathbf{D} \cdot \hat{\mathbf{N}} d\Gamma_D. \quad (15)$$

we finally obtain

$$P_m = -(A_{mi} + \gamma_{mi})^{-1}(\phi_{,i} + 2\tilde{f}\chi_i + d_{ijk}\epsilon_{jk} + m_{ij}a_j) \quad (16)$$

and

$$\begin{aligned} D_m &= \epsilon_0 E_m + P_m = -\epsilon_0 \phi_{,m} - (A_{mi} + \gamma_{mi})^{-1}(\phi_{,i} + 2\tilde{f}\chi_i + d_{ijk}\epsilon_{jk} + m_{ij}a_j) \\ &= -\Big(\epsilon_0 \delta_{mi} + (A_{mi} + \gamma_{mi})^{-1}\Big)\phi_{,i} - (A_{mi} + \gamma_{mi})^{-1}(2\tilde{f}\chi_i + d_{ijk}\epsilon_{jk} + m_{ij}a_j) \end{aligned} \quad (17)$$

Then, we have

$$\begin{aligned} &-\Big(\epsilon_0\delta_{mi} + (A_{mi} + \gamma_{mi})^{-1}\Big)\int_\Omega \phi_{,i}\delta\phi_{,m} d\Omega \\ &\quad - (A_{mi} + \gamma_{mi})^{-1}\int_\Omega (2\tilde{f}\chi_i + d_{ijk}\epsilon_{jk} + m_{ij}a_j)\delta\phi_{,m} d\Omega \\ &= \int_\Omega \tilde{\rho}\delta\phi d\Omega \int_{\partial\Omega} D_i \hat{N}_i \delta\phi d\Gamma_D \end{aligned} \quad (18)$$

In this work, the dynamics due to polarization γ_{ij} is neglected for two reasons:

- Different from the micro-inertia length scale related to the higher mechanical dispersion, the dynamics of polarization γ_{ij} is related to the higher electrical dispersion. In some applications such as energy harvesting, the mechanical loading is related to the direct flexoelectric effect rather than converse effect due to an applied electrical field.
- There has been no work until now measuring or theoretically evaluating the value of γ.

3 Time integration and Newton iterative solver

In order to solve the nonlinear dynamic equations (12), (18), we consider equilibrium at time step $t = n + 1$:

$$\begin{cases} f^d(a_i^{n+1}, \delta u_i^{n+1}) + f^m(u_i^{n+1}, \delta u_i^{n+1}) + f^e(u_i^{n+1}, \delta u_i^{n+1}, \phi^{n+1}) \\ \quad = f^{ext}(\delta u_i^{n+1}, \tilde{b}_i^{n+1}, \tau_i^{n+1}), & \text{(19a)} \\ h^e(\phi^{n+1}, \delta\phi^{n+1}) + h^m(u_i^{n+1}, \delta\phi^{n+1}) \\ \quad = h^{ext}(\delta\phi^{n+1}, D_i^{n+1}), & \text{(19b)} \end{cases}$$

with

$$\begin{aligned} f^d(a_i^{n+1}, \delta u_i^{n+1}) &= \int_\Omega \rho a_i^{n+1}\delta u_i^{n+1} d\Omega + \int_\Omega l^2 \rho a_{i,j}^{n+1}\delta u_{i,j}^{n+1} d\Omega, \\ f^m(u_i^{n+1}, \delta u_i^{n+1}) &= \int_\Omega (\sigma_{ij}^m)^{n+1}\delta\epsilon_{ij}^{n+1} d\Omega + \int_\Omega (s_i^a)^{n+1}\delta\chi_i^{n+1} d\Omega + \int_\Omega (s_{ij}^s)^{n+1}\delta\kappa_{ij}^{n+1} d\Omega, \\ f^e(u_i^{n+1}, \delta u_i^{n+1}, \phi^{n+1}) &= \int_\Omega P_i^{n+1}(2\tilde{f}\delta\chi_i^{n+1} + d_{ijk}\delta\epsilon_{jk}^{n+1}) d\Omega + \int_\Omega m_{ij}\ddot{P}_i^{n+1}\delta u_j^{n+1} d\Omega, \\ f^{ext}(\delta u_i^{n+1}, \tilde{b}_i^{n+1}, t_i^{n+1}, \tau_i^{n+1}) &= \int_\Omega \tilde{b}_i^{n+1}\delta u_i^{n+1} d\Omega + \int_{\partial\Omega} (t_i^{n+1} + \tau_i^{n+1})\delta u_i^{n+1} d\Gamma, \\ h^e(\phi^{n+1}, \delta\phi^{n+1}) &= (\epsilon_0\delta_{mi} + A_{mi}^{-1}) \int_\Omega \phi_{,i}^{n+1}\delta\phi_{,m}^{n+1} d\Omega, \\ h^m(u_i^{n+1}, \delta\phi^{n+1}) &= A_{mi}^{-1}\int_\Omega (2\tilde{f}\chi_i^{n+1} + d_{ijk}\epsilon_{jk}^{n+1} + m_{ij}a_j^{n+1})\delta\phi_{,m}^{n+1} d\Omega, \end{aligned}$$

$$h^{ext}(\delta\phi^{n+1}, D_i^{n+1}) = \int_\Omega \tilde{\rho}\delta\phi^{n+1}d\Omega - \int_{\partial\Omega} D_i^{n+1}\hat{N}_i\delta\phi^{n+1}d\Gamma_D \quad (20)$$

We take advantage of the implicit Newmark scheme [53,54] to update the velocity v_i and the acceleration a_i:

$$\begin{aligned} v_i^{n+1} &= v_i^n + \Delta t(1-\gamma)a_i^n + \gamma\Delta t a_i^{n+1}, \\ a_i^{n+1} &= \frac{1}{\Delta t^2\beta}u_i^{n+1} - g_i^n(u_i^n, v_i^n, a_i^n), \\ g_i^n(u_i^n, v_i^n, a_i^n) &= \frac{1}{\Delta t^2\beta}\Big(u_i^n + \Delta t v_i^n + \Delta t^2(0.5-\beta)a_i^n\Big), \end{aligned} \quad (21)$$

where the parameters of the Newmark scheme are chosen as $\beta = 1/4$ and $\gamma = 1/2$. Similarly, the polarization vector is approximated as

$$\begin{aligned} \dot{P}_i^{n+1} &= \dot{P}_i^n + \Delta t(1-\gamma)\ddot{P}_i^n + \gamma\Delta t\ddot{P}_i^{n+1}, \\ \ddot{P}_i^{n+1} &= \frac{1}{\Delta t^2\beta}P_i^{n+1} - g_i^n(P_i^n, \dot{P}_i^n, \ddot{P}_i^n). \end{aligned} \quad (22)$$

Linearization of above equations yields

$$\begin{aligned} &\Delta_u f^d(u_i^{n+1}, \delta u_i^{n+1}) + \Delta_u f^m(u_i^{n+1}, \delta u_i^{n+1}) \\ &\quad + \Delta_u f^e(u_i^{n+1}, \delta u_i^{n+1}, \phi^{n+1}) \\ &\quad + \Delta_\phi f^e(u_i^{n+1}, \delta u_i^{n+1}, \phi^{n+1}) \\ &= f^{ext}(\delta u_i^{n+1}, \tilde{b}_i^{n+1}, t_i^{n+1}, \tau_i^{n+1}), \\ &\quad - f^d(a_i^{n+1}, \delta u_i^{n+1}) - f^m(u_i^{n+1}, \delta u_i^{n+1}) \\ &\quad - f^e(u_i^{n+1}, \delta u_i^{n+1}, \phi^{n+1}) \\ &\Delta_\phi h^e(\phi^{n+1}, \delta\phi^{n+1}) + \Delta_u h^m(u_i^{n+1}, \delta\phi^{n+1}) \\ &= h^{ext}(\delta\phi^{n+1}, D_i^{n+1}) - h^e(\phi^{n+1}, \delta\phi^{n+1}) \\ &\quad - h^m(u_i^{n+1}, \delta\phi^{n+1}), \end{aligned}$$

where Δ_u and Δ_ϕ are the linearization operators with respect to u_i^{n+1} and ϕ_i^{n+1}, respectively, and

$$\begin{aligned} \Delta_u f^d(u_i^{n+1}, \delta u_i^{n+1}) &= \frac{1}{\Delta t^2\beta}\Big(\int_\Omega \rho\Delta u_i^{n+1}\delta u_i^{n+1}d\Omega \\ &\quad + \int_\Omega l^2\rho\Delta u_{i,j}^{n+1}\delta u_{i,j}^{n+1}d\Omega\Big) \\ &= \delta\mathbf{u}^{n+1}\mathbf{M}\Delta\mathbf{u}^{n+1}, \\ \Delta_u f^m(u_i^{n+1}, \delta u_i^{n+1}) &= \int_\Omega \Delta(\sigma_{ij}^m)^{n+1}\delta\epsilon_{ij}^{n+1}d\Omega \\ &\quad + \int_\Omega \Delta(s_i^a)^{n+1}\delta\chi_i^{n+1}d\Omega \\ &\quad + \int_\Omega \Delta(s_{ij}^s)^{n+1}\delta\kappa_{ij}^{n+1}d\Omega \\ &\quad + \int_\Omega (\sigma_{ij}^m)^{n+1}\Delta\delta\epsilon_{ij}^{n+1}d\Omega \\ &\quad + \int_\Omega (s_i^a)^{n+1}\Delta\delta\chi_i^{n+1}d\Omega \\ &\quad + \int_\Omega (s_{ij}^s)^{n+1}\Delta\delta\kappa_{ij}^{n+1}d\Omega \\ &= \delta\mathbf{u}^{n+1}\mathbf{K}^m(\mathbf{u}^{n+1})\Delta\mathbf{u}^{n+1}, \end{aligned}$$

$$\begin{aligned} &\Delta_u f^e(u_i^{n+1}, \delta u_i^{n+1}, \phi^{n+1}) + \Delta_\phi f^e(u_i^{n+1}, \delta u_i^{n+1}, \phi^{n+1}) \\ &= \int_\Omega P_i^{n+1}(2\tilde{f}\Delta\delta\chi_i^{n+1} + d_{ijk}\Delta\delta\epsilon_{jk}^{n+1})d\Omega \\ &\quad + \int_\Omega \Delta_u P_i^{n+1}(2\tilde{f}\delta\chi_i^{n+1} + d_{ijk}\delta\epsilon_{jk}^{n+1})d\Omega \\ &\quad + \int_\Omega \frac{m_{ij}}{\Delta t^2\beta}\Delta_u P_i^{n+1}\delta u_j^{n+1}d\Omega \\ &\quad + \int_\Omega \Delta_\phi P_i^{n+1}(2\tilde{f}\delta\chi_i^{n+1} + d_{ijk}\delta\epsilon_{jk}^{n+1})d\Omega \\ &\quad + \int_\Omega \frac{m_{ij}}{\Delta t^2\beta}\Delta_\phi P_i^{n+1}\delta u_j^{n+1}d\Omega \\ &= \delta\mathbf{u}^{n+1}\mathbf{K}^e(\mathbf{u}^{n+1}, \phi^{n+1})\Delta\mathbf{u}^{n+1} \\ &\quad + \delta\mathbf{u}^{n+1}\mathbf{K}_{u\phi}(\mathbf{u}^{n+1})\Delta\phi^{n+1}, \end{aligned} \quad (23)$$

$$\begin{aligned} \Delta_\phi h^e(\phi^{n+1}, \delta\phi^{n+1}) &= (\epsilon_0\delta_{mi} + A_{mi}^{-1})\int_\Omega \Delta\phi_{,i}^{n+1}\delta\phi_{,m}^{n+1}d\Omega \\ &= \delta\boldsymbol{\phi}^{n+1}\mathbf{K}_{\phi\phi}\Delta\boldsymbol{\phi}^{n+1}, \\ \Delta_u h^m(u_i^{n+1}, \delta\phi^{n+1}) &= A_{mi}^{-1}\int_\Omega (2\tilde{f}\Delta\chi_i^{n+1} \\ &\quad + d_{ijk}\Delta\epsilon_{jk}^{n+1} + \frac{m_{ij}}{\delta t^2\beta}\Delta u_j^{n+1})\delta\phi_{,m}^{n+1}d\Omega \\ &= \delta\boldsymbol{\phi}^{n+1}\mathbf{K}_{\phi u}(\mathbf{u}^{n+1})\Delta\mathbf{u}^{n+1}. \end{aligned}$$

Let's denote $\mathbf{K}_{uu}^{n+1} = \mathbf{K}^m(\mathbf{u}^{n+1}) + \mathbf{K}^e(\mathbf{u}^{n+1}, \boldsymbol{\phi}^{n+1})$, $\mathbf{K}_{u\phi}^{n+1} = \mathbf{K}_{u\phi}(\mathbf{u}^{n+1})$ and $\mathbf{K}_{\phi u}^{n+1} = \mathbf{K}_{\phi u}(\mathbf{u}^{n+1})$. Rayleigh damping, which is a linear combination of the mass and the stiffness matrices, is applied $\tilde{\mathbf{D}}_{uu}^{n+1} = \alpha_1\mathbf{K}_{uu}^{n+1} + \alpha_2\mathbf{M}$ where

$$\begin{bmatrix}\alpha_1 \\ \alpha_2\end{bmatrix} = \frac{2\omega_1\omega_2}{\omega_1^2 - \omega_2^2}\begin{bmatrix}1/\omega_2 & -1/\omega_1 \\ -\omega_2 & \omega_1\end{bmatrix}\begin{bmatrix}\xi_1 \\ \xi_2\end{bmatrix} \quad (24)$$

and ξ_1 and ξ_2 are two damping ratios. The Newton–Raphson iterative is used to solve the linearized system of equations, i.e.,

$$\begin{aligned} &\begin{bmatrix}\mathbf{K}_{uu,k}^{n+1} + \gamma\frac{\tilde{\mathbf{D}}_{uu,k}^{n+1}}{\beta\Delta t} + \frac{\mathbf{M}}{\beta\Delta t^2} & \mathbf{K}_{u\phi,k}^{n+1} \\ \mathbf{K}_{\phi u,k}^{n+1} & \mathbf{K}_{\phi\phi,k}\end{bmatrix}\begin{bmatrix}\Delta\mathbf{u}_{k+1}^{n+1} \\ \Delta\boldsymbol{\phi}_{k+1}^{n+1}\end{bmatrix} \\ &= \begin{bmatrix}\mathbf{f}_u^{n+1} - \mathbf{R}_{u,k}^{n+1} - \tilde{\mathbf{D}}_{uu}^{n+1}\tilde{\mathbf{v}}_k^{n+1} - \mathbf{M}\tilde{\mathbf{a}}_k^{n+1} \\ \mathbf{f}_\phi^{n+1} - \mathbf{R}_{\phi,k}^{n+1}\end{bmatrix} \end{aligned} \quad (25)$$

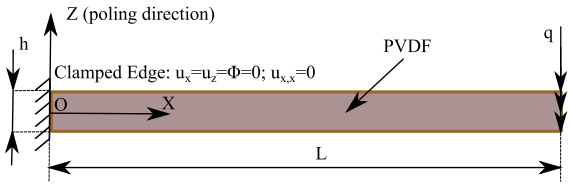

Fig. 1 Bending cantilever beam

where $\mathbf{f}_u^{n+1} \cdot \delta\mathbf{u}^{n+1} = f^{ext}$, $\mathbf{f}_\phi^{n+1} \cdot \delta\boldsymbol{\phi}^{n+1} = h^{ext}$, $\mathbf{R}_{u,k}^{n+1} \cdot \delta\mathbf{u}^{n+1} = f^m + f^e$, $\mathbf{R}_{\phi,k}^{n+1} \cdot \delta\boldsymbol{\phi}^{n+1} = h^m + h^e$. The IGA-based spatial discretization can be found in Appendix B. In this work, quadratic NURBS functions are implemented for all numerical examples.

4 Numerical examples

4.1 Linear analysis for cantilever beam: analytical solution vs. numerical solution

Let us consider a cantilever beam subjected to distributed bending force q = 1N/m as illustrated in Fig. 1. The beam is clamped on its left edge with $u_x = u_z = \phi = 0$ and $u_{x,x} = 0$ (C^1 continuity condition). The material parameters of polyvinylidene difluoride (PVDF) from Table 1 are adopted; the beam's dimensions are as follows: h=10^{-6}m, L=50h. The shear modulus is assumed to be zero for a comparative study between numerical results and analytical solutions which are obtained from beam theory as

$$u_y(x) = w(x) = \frac{2qx^2(-3L+x)\alpha_{33}}{c_{11}h^3\alpha_{33} - 12\tilde{f}^2h(\alpha_{33}-\epsilon_0)\alpha_{33} - d_{33}^2h^3(\alpha_{33}-\epsilon_0) + 12h(g_1+4g_2)\alpha_{33}},$$
$$\phi(x) = -\frac{h}{2}\frac{12e^{-x/z}\tilde{f}q(L - e^{x/z}L + e^{x/z}(x-z) + z)(\alpha_{33}-\epsilon_0)}{c_{11}h^3\alpha_{33} - 12\tilde{f}^2h(\alpha_{33}-\epsilon_0)\alpha_{33} - d_{33}^2h^3\epsilon_0(\alpha_{33}-\epsilon_0) + 12h(g_1+4g_2)\alpha_{33}}. \quad (26)$$

Figure 2 shows excellent agreement between the analytical solutions and numerical results. In the following numerical example, we will illustrate the limit of the beam model and the need for our proposed two-dimensional approach—especially for analyzing the vibration behavior.

4.2 Relation of natural frequencies and sample thickness

Many previous works have pointed out the dominance of the flexoelectric effect over the piezoelectric effect at the micro-scale [32,35]. To accurately capture the flexodynamic effect at lower scale, the eigenfrequencies should be evaluated properly. The variation of the first eigenfrequency of the cantilever beam from Fig. 3 with respect to sample thickness is investigated. The material parameters of $SrTiO_3$ from Table 2 with $g_2 = 0$ are chosen in order to verify our 2D model with the reduced-order beam formulation from Deng et al. [34] where the ratio L/W/h are fixed to be 20/1/1 for all values of thickness h. The results are illustrated in Fig. 4; for h > 20 nm, the beam and 2D models give nearly same values for f. However, when h ≤ 10 nm, the discrepancy of the two models increase from 23.31 to 33.35 and 44.09% for h = 10 nm, h = 7 nm and h = 5 nm, respectively, suggesting the beam model overestimates the natural frequency.

4.3 Linear analysis for frequency response and external electrical circuit condition

If the external mechanical excitation is harmonic, i.e., $\mathbf{f}_u(t) = \bar{\mathbf{f}}_u Exp(I\omega t)$ and $\mathbf{f}_\phi(t) = 0$, the solutions have the form $\mathbf{u} = \bar{\mathbf{u}}_0 Exp(I\omega t)$ and $\boldsymbol{\phi} = \bar{\boldsymbol{\phi}}_0 Exp(I\omega t)$ where $\bar{\mathbf{u}}_0$ and $\bar{\boldsymbol{\phi}}_0$ are obtained from

$$\begin{bmatrix} \bar{\bar{\bar{\mathbf{K}}}}_{uu}\omega^4 - (\mathbf{M} + \bar{\bar{\mathbf{K}}}_{uu})\omega^2 + I\mathbf{D}\omega + \bar{\mathbf{K}}_{uu} & -\bar{\bar{\mathbf{K}}}_{u\phi}\omega^2 + \bar{\mathbf{K}}_{u\phi} \\ -\bar{\bar{\mathbf{K}}}_{\phi u}\omega^2 + \bar{\mathbf{K}}_{\phi u} & \mathbf{K}_{\phi\phi} \end{bmatrix} \begin{bmatrix} \bar{\mathbf{u}}_0 \\ \bar{\boldsymbol{\phi}}_0 \end{bmatrix} = \begin{bmatrix} \bar{\mathbf{f}}_u \\ \mathbf{0} \end{bmatrix}. \quad (27)$$

Detailed expressions for $\bar{\mathbf{K}}_{uu}$, $\bar{\bar{\mathbf{K}}}_{uu}$, $\bar{\bar{\bar{\mathbf{K}}}}_{uu}$ are presented in Appendix C. If the beam operates as a capacitor and is connected to an external electrical resistance, the rate of the average electrical displacement $D_3 = -\epsilon_0\frac{\partial\phi}{\partial\xi^3} + P_3$ over the thickness can be expressed as a current flow through the resistor by Gauss law

$$\frac{V}{R} + \epsilon\frac{w}{h}\dot{V}L = -w(\epsilon-\epsilon_0)\int_\Omega (\tilde{f}\dot{\chi}_i + d_{ijk}\dot{\epsilon}_{jk} + m_{ij}\dot{a}_j)d\Omega \quad (28)$$

With an input harmonic loading, equation (28) is rewritten as

Table 1 Material properties of PVDF

Material parameter	Symbol	Value
Elastic coefficients	$C_{11} \approx C_{22}$	3.61 [GPa] [55]
	C_{33}	1.63 [GPa] [55]
	$C_{13} \approx C_{12} \approx C_{23}$	1.42 [GPa] [55]
	$C_{44} \approx C_{55} \approx C_{66}$	0.55 [GPa] [55]
	$l_1 = l_2$	5×10^{-7} [m][32]
Permittivity	$\alpha_{11} \approx \alpha_{33}$	$7.55\epsilon_0$ [F/m] [55]
	α_{22}	$9.27\epsilon_0$ [F/m] [55]
Flexoelectric coefficients	$\tilde{f} = \frac{f_{12}-f_{44}}{2}$	1.3×10^{-8} [C/m] [56]
Piezoelectric coefficients	d_{31}	0.21 [Vm/N] [55]
	d_{33}	−0.46 [Vm/N] [55]
Mass density	ρ	1780 [kg/m^3] [32]
Damping ratio	ζ_r	0.05

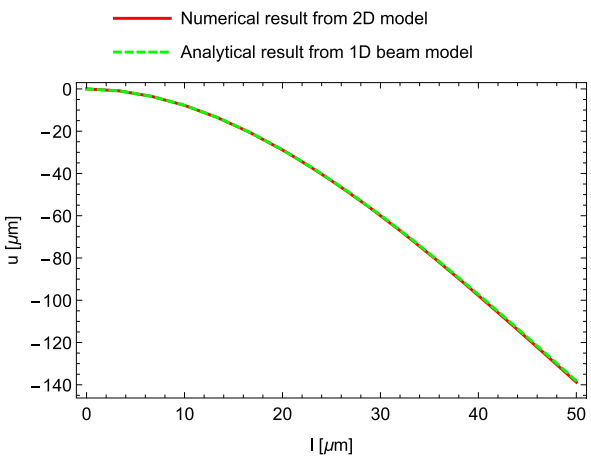

a Displacement u_z at middle line

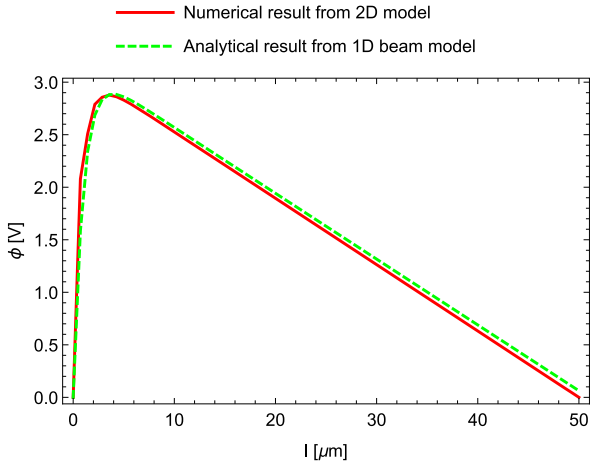

b Electric potential ϕ over the thickness

Fig. 2 Cantilever beam analytical results vs. numerical results

$$\frac{V}{R} + \epsilon \frac{w}{h} \dot{V} L = -w(\epsilon - \epsilon_0) \int_\Omega (I\omega \tilde{f} \bar{\chi}_i + I\omega d_{ijk} \bar{\epsilon}_{jk} - I\omega^3 m_{ij} \bar{u}_j) d\Omega. \quad (29)$$

and the power density is computed as

$$\bar{P} = \frac{V^2}{R \int_\Omega d\Omega} \quad (30)$$

Let us consider the frequency response of the base excitation beam from Fig. 3. The same material parameters are used as in Sect. 4.2. The thickness $h = 10$ nm, the length $L = 20$ h, the amplitude of excitation is set equal $w_0 = 9.81/\omega_1^2$ as in [33] with $\omega_1 = 2\pi f_1^e$. To

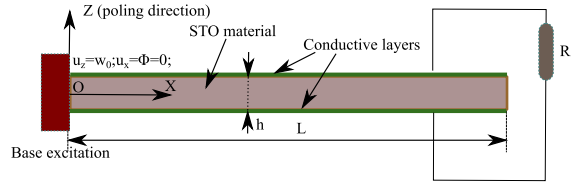

Fig. 3 Cantilever beam-based energy harvester

study the influences of different material inputs on the output of the energy harvester, a sensitivity analysis is carried out. The influence of the flexoelectric coefficient $\tilde{f}$ is presented in Fig. 5. Increasing the magnitude

Table 2 Material properties of $SrTiO_3$

Material parameter	Symbol	Value
Elastic coefficients	$C_{11} = C_{22} = C_{33}$	317.2 [GPa] [57]
	$C_{12} = C_{23} = C_{13}$	102.5 [GPa] [57]
	$C_{44} = C_{55} = C_{66}$	123.5 [GPa] [57]
	$l_1 = l_2$	1.0×10^{-8} [m] [34]
Permittivity	$\alpha_{11} \approx \alpha_{22} \approx \alpha_{33}$	$240\epsilon_0$ [F/m] [52,58]
Flexoelectric coefficients	$\tilde{f} = \frac{f_{12} - f_{44}}{2}$	−0.51 [Nm/C] [52]
Piezoelectric coefficients	d_{31}	6.1 [pm/V] [59]
	d_{33}	40.0 [pm/V] [59]
Mass density	ρ	5174 [kg/m^3] [52]
Damping ratio	ζ_r	0.05

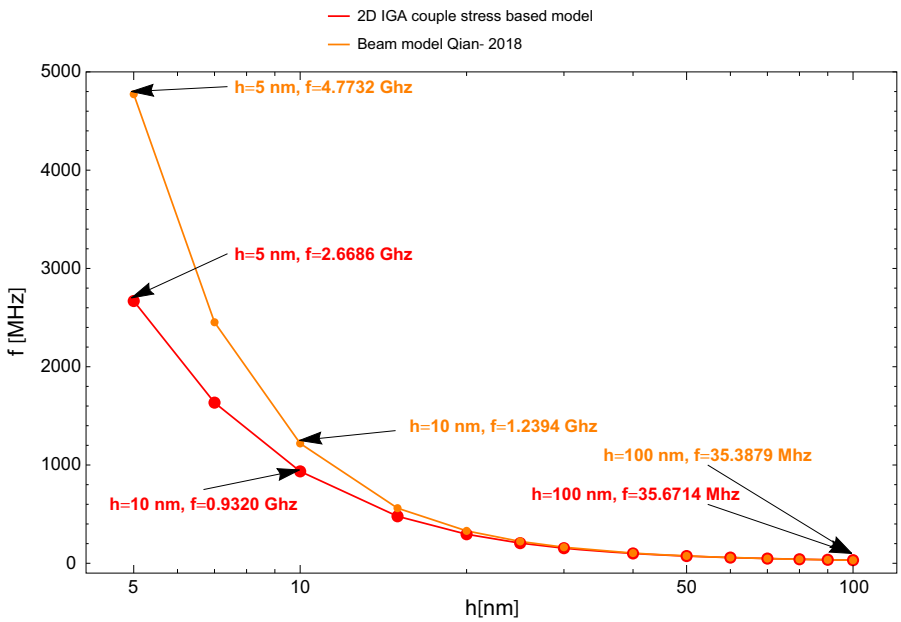

Fig. 4 Comparison between Euler–Bernoulli beam model and 2D IGA-based model on the variation of first eigenfrequency f with respect to the beam thickness h. The ratio L/W/h are fixed to be 20/1/1 for all values of thickness h

of $\tilde{f}$ from 0.3 to 2.3 Nm/C (7.76 times) makes the voltage and power density increase 41.32 times and 1707.4 times, respectively. This agrees with Eq. (30) where the power is a quadratic function of voltage. Figure 5 shows a direct relation between the flexoelectric parameter $\tilde{f}$ and the electrical outputs. As we can see, higher values of $\tilde{f}$ give higher voltages and powers; this indicates the importance of seeking higher flexoelectric effect materials for practical applications [60] in order to improve the performance of energy harvester. The effect of the electrical circuit boundary condition with the variation of electrical resistance R can be found in Fig. 6. Increasing the electrical resistance R from 10 to 500 KΩ makes the outcome voltage increases from 1.37×10^{-9}μV to 3.24×10^{-8}μV and this totally agrees with Eq. (29). For each value of R, the peaks of output voltage and power density of frequency response curves are obtained at the natural frequency $f_1^e = 1.394$ GHz. When connecting with an external electric circuit, the beam plays as a capacitor and the external electrical resistance R contributes to the system admittance $j\omega C + 1/R$ where C is the beam's capacitor. Hence, it does not exhibit a monotonic behavior of the power density when increasing (or decreasing) the load resistance according to Eqs. (29) and (30). To be precise, increasing the electrical resistance R from 10 to 250 KΩ

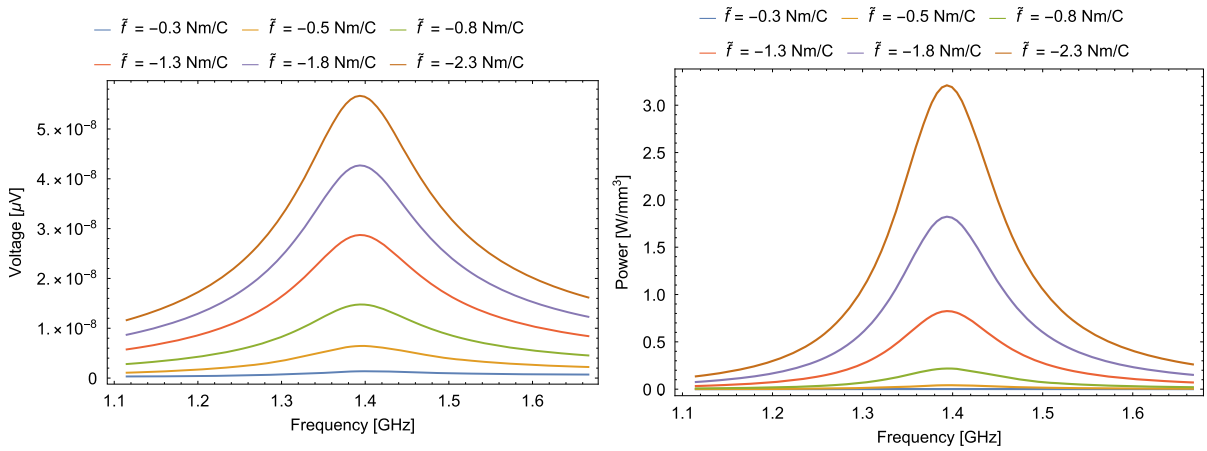

a Voltage response **b** Power density response

Fig. 5 Effect of flexoelectricity with variation of f, $l_d = 10\,\text{h}$, $R = 50\,\text{K}\Omega$ and $m = 6 \times 10^{-8}\ \text{Vs}^2/\text{m}^2$

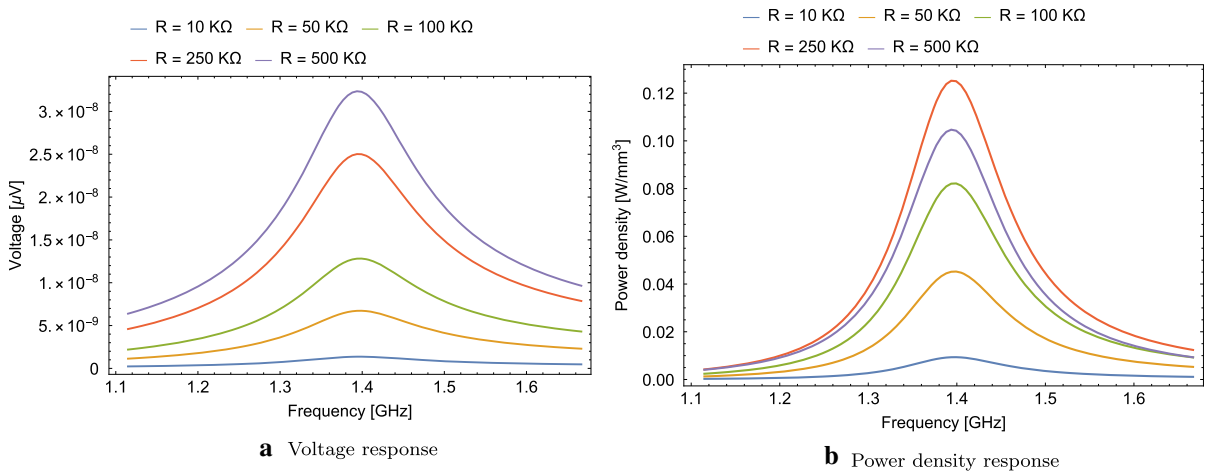

a Voltage response **b** Power density response

Fig. 6 Effect of electrical circuit boundary condition with variation of R, $l_d = 10\,\text{h}$ and $m = 6 \times 10^{-8}\ \text{Vs}^2/\text{m}^2$

lead the power increases from 0.01 to $0.125\,\text{W/mm}^3$. However, when $R = 500\,\text{K}\Omega$ the power is decreased to $0.105\,\text{W/mm}^3$. In this case, $R = 250\,\text{K}\Omega$ is the optimal value of the electrical resistance. In practical applications, it is important to find the optimal value of R where the power density of energy harvesting structure is maximized. The influence of the flexodynamic effect on the frequency response is illustrated in Fig. 7 by varying the flexodynamic parameter m from $4 \times 10^{-8}\text{Vs}^2/\text{m}^2$ to $7 \times 10^{-8}\text{Vs}^2/\text{m}^2$; this is studied with three cases of nonlocal elastic parameters $g_1 = g_2 = h$, $g_1 = g_2 = 1.3h$ and $g_1 = g_2 = 1.7h$. It can be observed from Fig. 7, the flexodynamic effect has an remarkable impact on the outputs of energy harvester. However, the behavior of the influence depends strongly on the elastic length scales. For the case $g_1 = g_2 = h$ (see Fig. 7a, b), the flexodynamicity diminishes the voltage and power density, i.e., higher values of m cause lower values V and $\bar{P}$. For the case $g_1 = g_2 = 1.7h$, the situation is opposite when the flexodynamic effect enhances the outputs, i.e., higher values of m give higher values V and $\bar{P}$ (see Fig. 7e, f). When $g_1 = g_2 = 1.3h$, it is observed that increasing m from $4 \times 10^{-8}\text{Vs}^2/\text{m}^2$ to $6 \times 10^{-8}\text{Vs}^2/\text{m}^2$ leads the voltage decrease from 3.13 to 1.25×10^{-9} μV. However increasing m from $6 \times 10^{-8}\text{Vs}^2/\text{m}^2$ to $7 \times 10^{-8}\text{Vs}^2/\text{m}^2$ makes an increase of the voltage from 1.25 to 1.93×10^{-9} μV (see Fig. 7c). Similar behavior is observed for the power (see Fig. 7d). Besides,

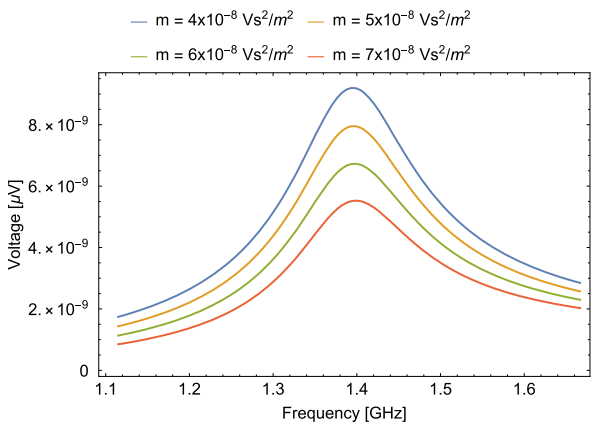

a Voltage response with $l_1 = l_2 = h$

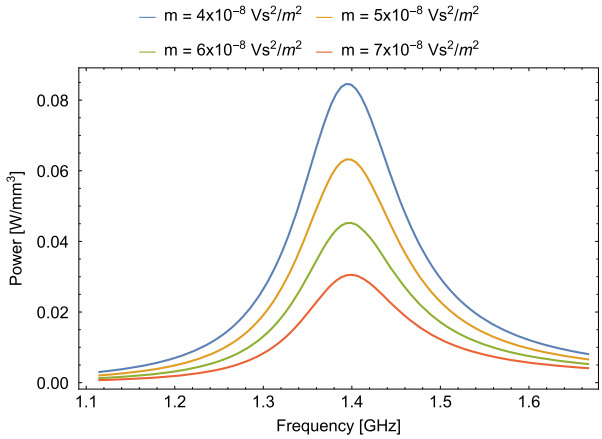

b Power density response with $l_1 = l_2 = h$

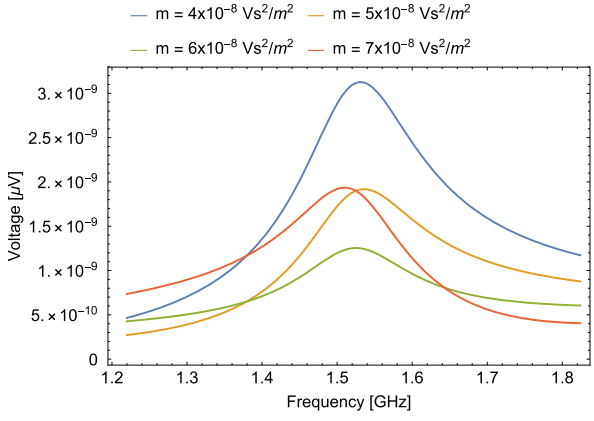

c Voltage response with $l_1 = l_2 = 1.3h$

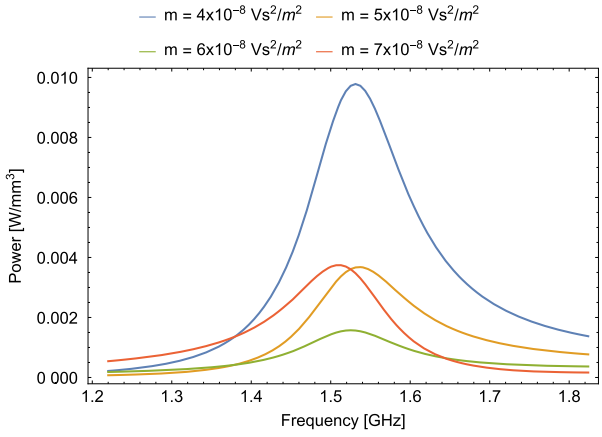

d Power density response with $l_1 = l_2 = 1.3h$

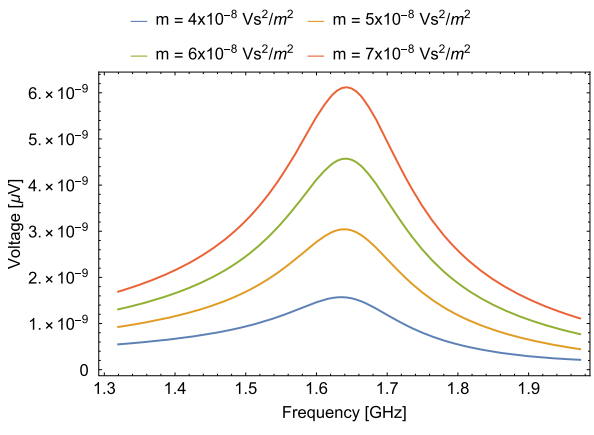

e Voltage response with $l_1 = l_2 = 1.7h$

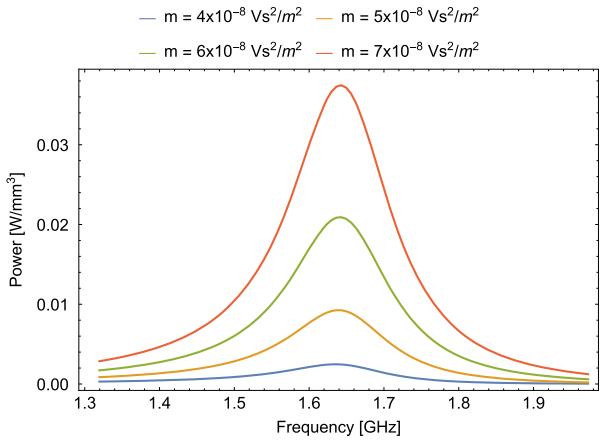

f Power density response with $l_1 = l_2 = 1.7h$

Fig. 7 Effect of flexoelectric-dynamics with variation of m, l_1 and l_2, $l_d = 10$ h and $R = 50$ KΩ

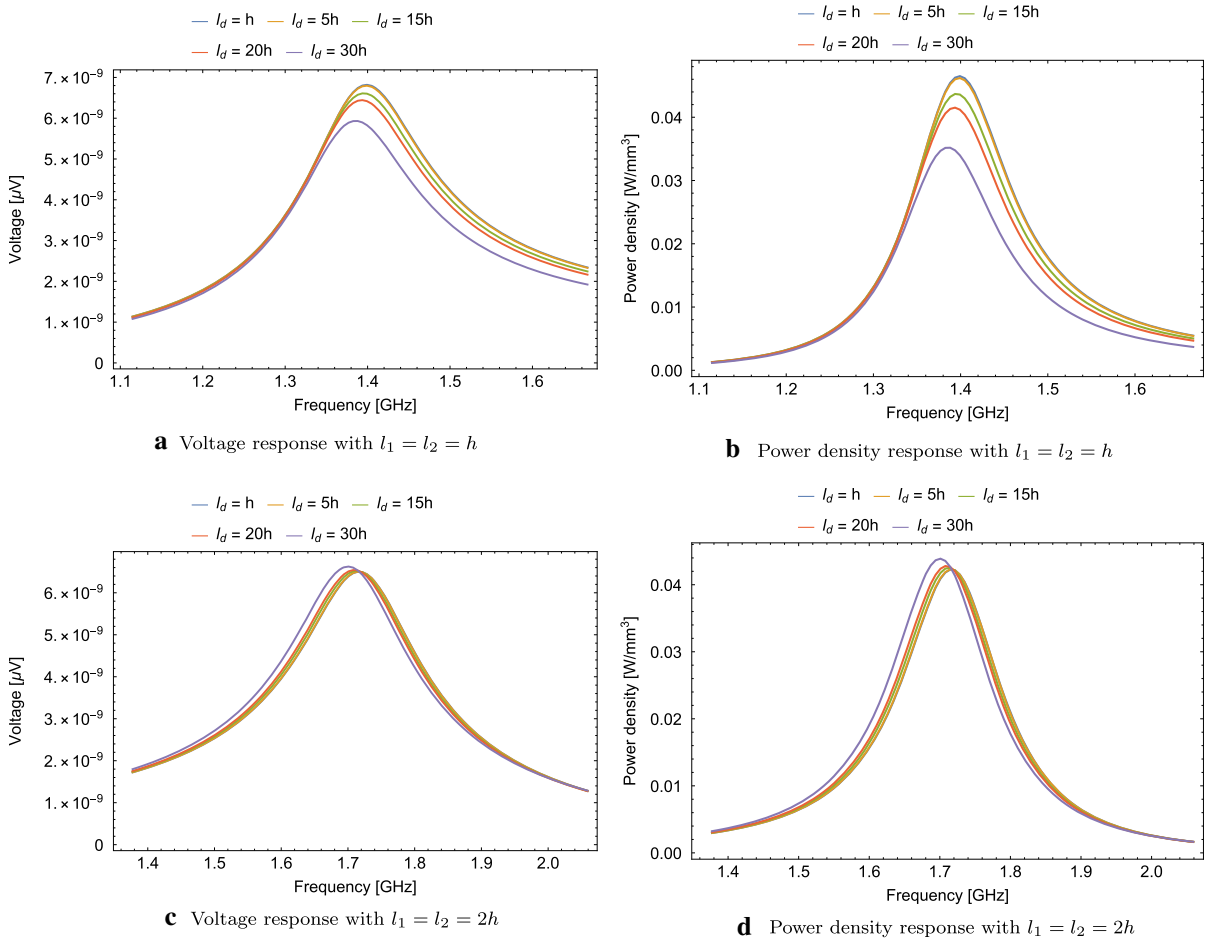

a Voltage response with $l_1 = l_2 = h$

b Power density response with $l_1 = l_2 = h$

c Voltage response with $l_1 = l_2 = 2h$

d Power density response with $l_1 = l_2 = 2h$

Fig. 8 Effect of micro-inertia effect with variation of l_d, l_1 and l_2, $m = 6 \times 10^{-8}$ Vs^2/m^2 and $R = 50$ KΩ

the maximum voltage and power density are found around the natural frequency for all values of m indicating that the flexoelectric dynamic effect does not affect the structural eigenfrequency. The micro-inertia effect is presented in Fig. 8 where l_d is varied from h to 30 h. Two values of the nonlocal elastic length scale, i.e., $g_1 = g_2 = h$ and $g_1 = g_2 = 2h$ are included in the study. When $g_1 = g_2 = h$ as illustrated in Fig. 8a, b, the magnitudes of voltage and power density get smaller with larger values of l_d. More importantly, we find—different from the flexodynamic effect—there is a shifting of the system's natural frequency when varying l_d. We note that the inclusion of the inertial-related length scale is necessary in order to capture the dispersive behavior of microstructures. When $g_1 = g_2 = 2$h (see Fig. 8c, d), it can be found that the first natural frequency f_1^e is increased from 1.39 GHz to 1.72 GHz; however, it also leads to less sensitivity of the outputs with respect to l_d. Many studies [61,62] have pointed out that the length scale should be small enough and directly related to the lattice space, it also depends on the correlation properties of the medium. It was shown from Askes et al. [63] that for the wave propagation of pulse loads, taking the ratio h/g_1 = h/g_2 = 1 and h/l_d = 1 are appropriate choices.

4.4 Nonlinear analysis: shoe-mounted flexoelectric energy harvester

Inspired from the well-known work on curved piezoelectric energy harvesters [64], we study a shoe-mounted micro-scale energy harvester as illustrated in Fig. 9. The heel strike compressing energy from

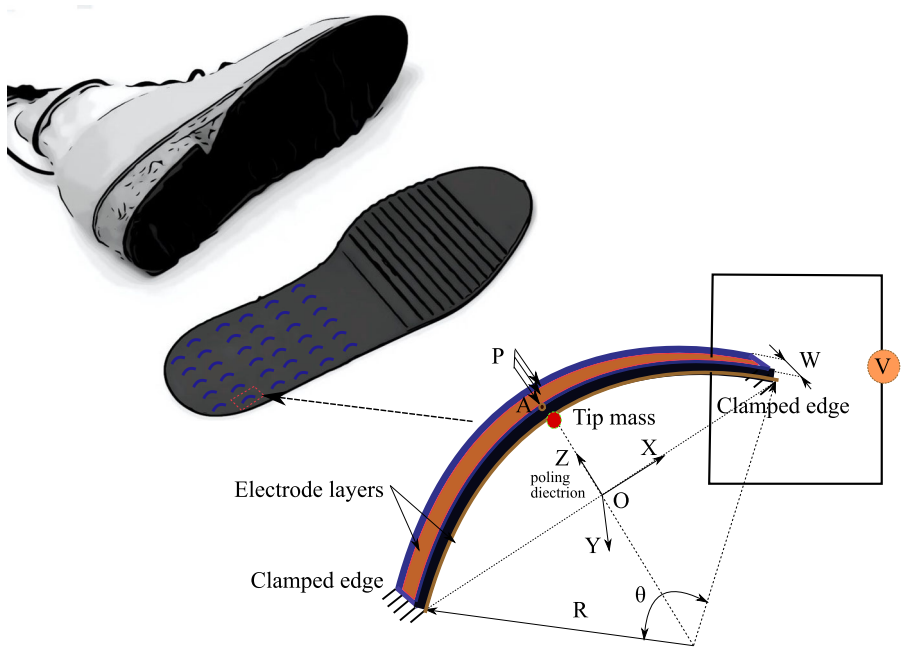

Fig. 9 Sketch illustrating of micro-scale shoe-mounted energy harvester. Layers of curved energy harvesting components are placed on the shoe insole to harness the heel strike energy

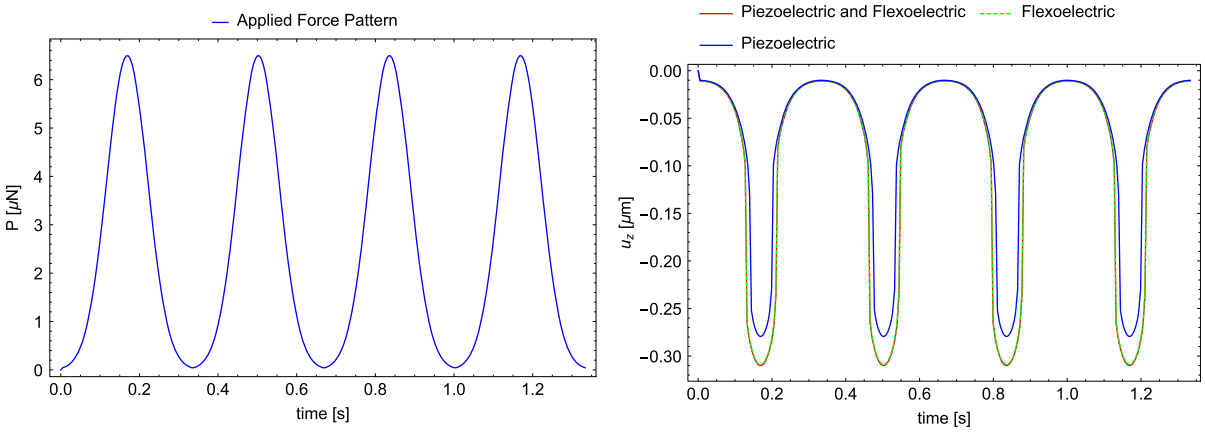

a Applied force pattern **b** Vertical displacement u_z

Fig. 10 Applied force pattern and resulting vertical displacement at point A for the case $f = 3$ Hz

the bending process of the foot is harvested by layers of curved energy harvesting components. Let us quantify the piezoelectric and flexoelectric effects on the energy conversion. The material parameters from Table 1 are adopted. Although PVDF materials belong to the orthorhombic mm2 symmetry, the experimental data from Roh et al. [55] show that at room temperature, the assumption of cubic behavior is still acceptable. A tip mass 4×10^{-8} kg is attached at the midspan at the lower edge (see Fig. 9), and the gravity forces of this tip mass and the beam are considered as well. The sizes of curved beam are as follows: curvature $r = 0.5$ μm, beam thickness $h = 6r/100$, width $w = 5r$ and central angle $\theta = 2.5\pi/4$. The flexodynamic coefficient is computed theoretically following Tagantsev [44], Yudin and Tagantsev [46] and Kvasov and Tagantsev [52] as $m_{ij} = \chi_{ij}\frac{m_2 - m_1}{2q}$. For PVDF-$\beta$ $(-CH_2 - CF_2-)_n$, we have $m_1 = 14u$, $m_2 = 50u$, $q = 1.602 \times 10^{-19}$ C is the elementary charge, u is the atomic mass, $u = 1.6605 \times 10^{-27}$ kg, and

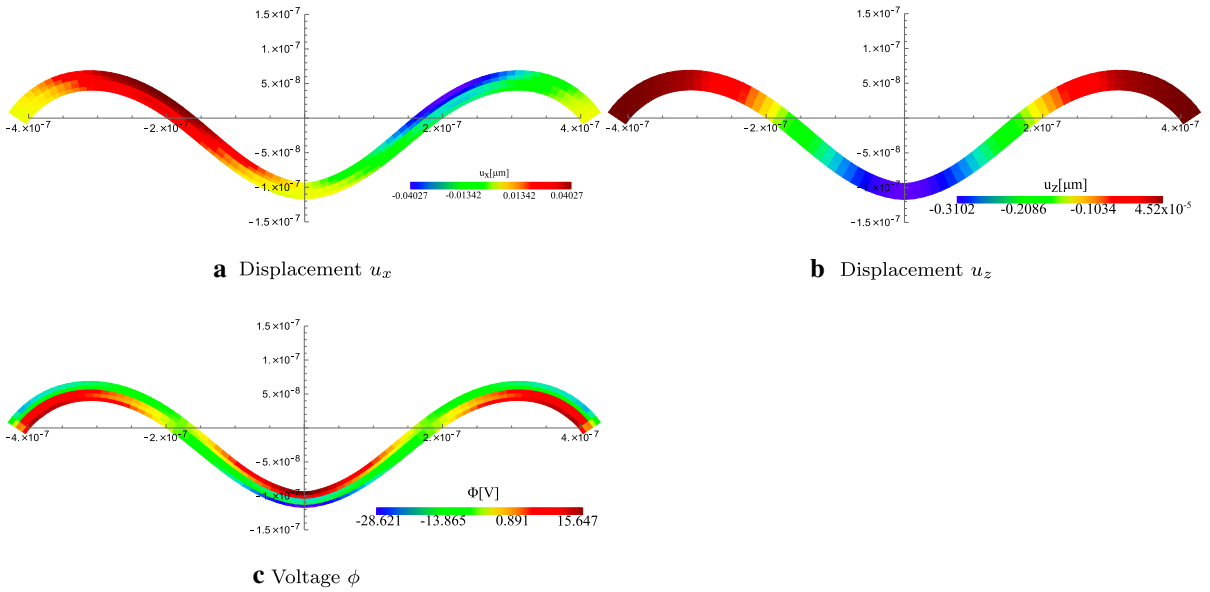

a Displacement u_x

b Displacement u_z

c Voltage ϕ

Fig. 11 Distribution of displacement and electric potential fields of shoe-mounted micro-scale energy harvester at maximum loading step $P = 6.5$ μN, $t = 1.17$ s

$\chi_{ij} = (\epsilon_r - 1)\delta_{ij}$ is the dielectric susceptibility hence $m_{ij} = 1.529 \times 10^{-6}\delta_{ij}$ Vs^{2}m^{-2}. Open electrical circuit conditions, i.e., $R \to \infty$ are assumed.

Figure 10a shows the force pattern imitating the applied force on the foot during the running process with $F = 3$ Hz and $P_{max} = 6.5$ μN. The impulse function of stepping process is assumed to have the form of Gaussian distribution, i.e., $P(t) = P_{max}e^{-t^2/2a^2}$ where a is the full width at half maximum and we choose $a^2 = 0.1$. The step frequency in human running is $f = 3$ Hz [65]. Figure 10b shows the vertical displacement u_z at the observed point A; a snap through occurs such that u_z jumps from -0.098 to -0.265 μm when P is about 4.71 μN. The full model including both piezoelectric and flexoelectric effects give nearly identical results as the model containing only flexoelectric effects; the piezoelectric model predicts only a slightly smaller value of maximum u_z. Distributions of the displacement field of shoe-mounted micro-scale energy harvesters at maximum load of $P = 6.5$ μN and $t = 1.172$ s are presented in Fig. 11a, b. The highest difference in the electric potential between the upper and lower layers is observed at the beam's mid-span where the loading force is applied (see Fig. 11c). The output voltage under open electrical circuit condition is shown in Fig. 12a. Before the snap through, in the first cycle, the voltage is positive and reaches a maximum of 0.324 mV at $t = 0.113$ s. The minimum voltage is -3.389 mV at $t = 0.172$ s after the snap through. This indicates that a higher voltage level can be obtained when operating the flexoelectric energy harvesting in the regime of finite displacement as the inhomogeneity of applied mechanical strain is enhanced. The minimum value of the voltage from piezoelectric material is -0.129 mV. Obviously, at smaller loads, the piezoelectric effect is nearly zero, larger loads make the strain over thickness inhomogeneous and the voltage related to the piezoelectricity over the thickness is nonzero. However, compared to the flexoelectric effect, the contribution of piezoelectricity is insignificant. Our results indicate that the flexoelectric effect dominates the electro-mechanical coupling effect at the micro-scale. The energy conversion factor is an important quantity for evaluating the efficiency of MEMS devices and computed as

$$\eta = \frac{\Pi_E^{n+1}}{W_F^{n+1}}, \tag{31}$$

where W_F^{n+1} denotes the external work and Π_E^{n+1} is the electrical energy at the time step $t = n + 1$. For energy harvesters, $h^{ext} = 0$ and we obtain

$$\begin{aligned} W_F^{n+1} &= f^{ext}(u_i^{n1+1}, \tilde{b}_i^{n+1}, \tau_i^{n+1}) = u_i^{n+1} K_{uu,ij}^{n+1} u_j^{n+1} \\ &\quad + u_i^{n+1} K_{u\phi,ij}^{n+1} \phi_j^{n+1} \\ &= u_i^{n+1} K_{uu,ij}^{n+1} u_j^{n+1} + \phi_i^{n+1} K_{\phi\phi,ij}^{n+1} \phi_j^{n+1} \end{aligned}$$

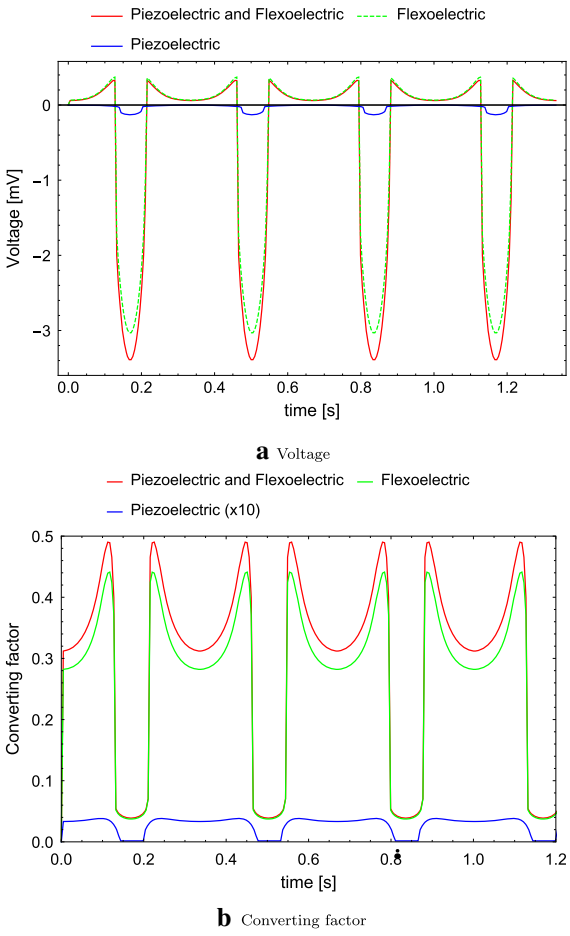

Fig. 12 Voltage and converting factor of the case $F = 3$ Hz. The coupling factor and voltage of the piezoelectric model are amplified by 10 times. The flexoelectric effect has a more significant contribution over the piezoelectric effect

$$= \Pi_S^{n+1} + \Pi_E^{n+1}, \tag{32}$$

with $\Pi_S^{n+1} = u_i^{n+1} K_{uu,ij}^{n+1} u_j^{n+1}$ and $\Pi_E^{n+1} = \phi_i^{n+1} K_{\phi\phi,ij}^{n+1} \phi_j^{n+1}$. The time-dependent energy conversion factor (ECF) in four cycles can be found in Fig. 12b for $F = 3$ Hz. In the first cycle, when the voltage obtains is maximum at $t = 0.113$ s, the ECF is also maximum with $\eta = 0.49$. At $t = 0.13$ s, the ECF is minimum, $\eta = 0.054$, when snap through is observed, indicating the main contribution of the flexoelectric effect to the electro-mechanical coupling. The voltage response of three different excited frequencies ($F = 3$ Hz, $F = 30$ Hz and $F = 60$ Hz) is presented in Fig. 13. Higher frequencies lead to higher inertia and dynamic effects which yields negative voltage in the first half cycle and increases the voltage magnitude in the remaining half

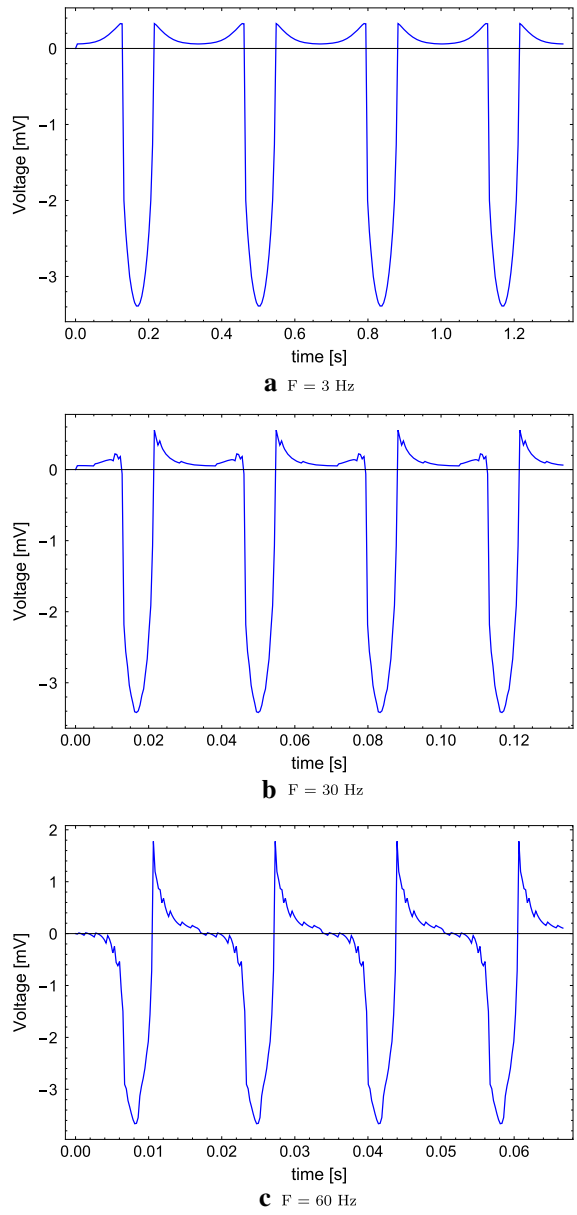

Fig. 13 Voltage response was observed in four cycles for three different exciting frequencies. It is observed that higher frequencies make the inertial effect more profound

cycle. The size effect is examined by varying the structural radius r, see Fig. 14. The voltage output is studied for five different values for r. Figure 14a from the piezo-flexoelectric model and Fig. 14b from the flexoelectric model are nearly identical due to the dominance of the flexoelectric effect at micro-scale. As pointed out in [66], the size effect influences the critical buckling

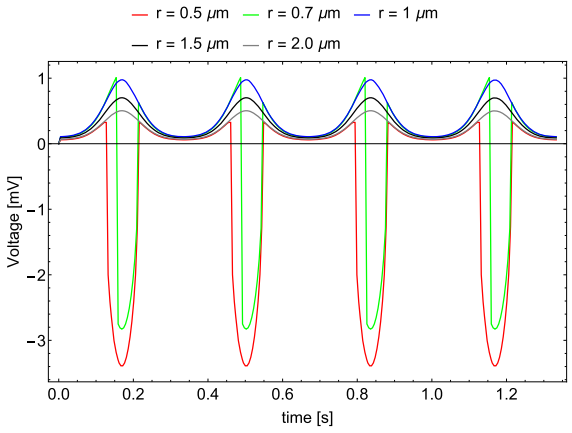

a Piezoelectric and flexoelectric model

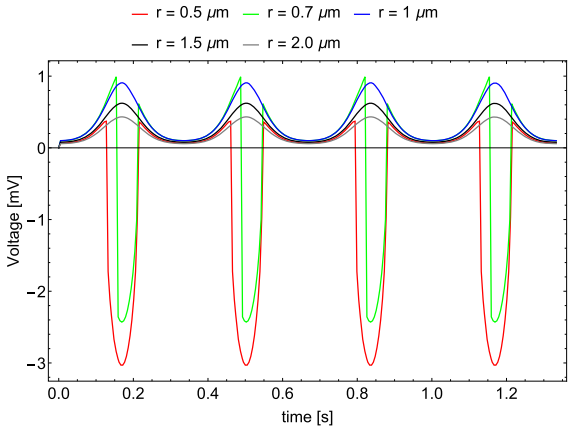

b Flexoelectric model

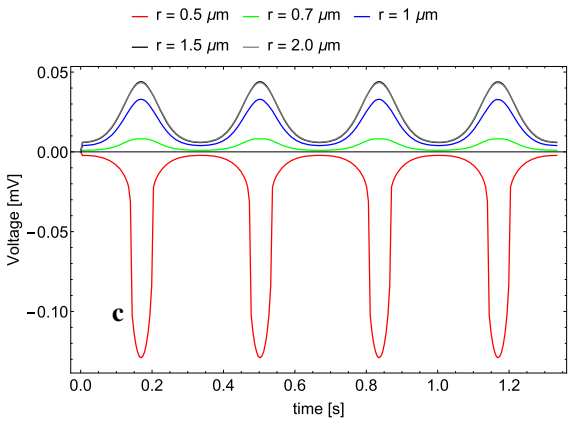

c Piezoelectric model

Fig. 14 Size effect: voltage response observed in four cycles for five different values of curvature r with $F = 3$ Hz

load. For $r = 0.5$ μm and $r = 0.7$ μm, the critical buckling values are 4.711 and 6.155 mN. The maximum absolute magnitude of the voltage is inversely proportional to r, with values of -3.39 and -2.268 mV for $r = 0.5$ μm and $r = 0.7$ μm, respectively. This is because for the cases of $r = 0.5$ μm and $r = 0.7$ μm, the structures become more compliant; hence, the snap-through effect happens with a smaller value of applied force. After the snap-through, the deformation is altered from compression to dilation; this leads to a redistribution of the strain and strain gradient. Consequently, the voltage sign and the polarization direction are changed. For larger values of r, the beam is stiffer; hence, the buckling effect does not occur such that the voltage does not change its sign. The maximum voltage values are 0.975, 0.701 and 0.503 mV for $r = 1.0$, 1.5, and 2.0 μm, respectively. In the full and the 'pure' flexoelectric models (see Fig. 14a, b), the maximum voltage decreases with increasing r. The situation is different for the piezoelectric model, see Fig. 14c. Larger values of r lead to higher maximum voltage levels confirming that increasing the structural dimensions increases the contribution of piezoelectricity and decreases the contribution of flexoelectricity.

5 Conclusions

In this work, we have developed a nonlinear dynamically consistent model to characterize the vibrational behavior of electro-mechanical coupling structures at the micro-scale by including size effects, flexoelectricity, and their corresponding dispersive behaviors, i.e., the internal inertia gradient effect and dynamic flexoelectric effect. We also studied the influence of these effects on the output of the flexoelectric energy harvester for both time and frequency responses. It is pointed out that decreasing the structural size not only diminishes the piezoelectric effect and enhances the flexoelectric effect but also increases the dynamic flexoelectric effect and the internal inertia gradient effect. The proposed model is expected to serve as a numerical tool in evaluating and characterizing the realistic dynamic behavior of MEMS and vibrational structures such as actuators and sensors.

For energy harvesting applications, the dynamic flexoelectric effect reduces the output voltage but does not notably influence the natural frequencies. The micro-inertia effect on the other hand shifts the natural

frequencies and increases the obtained output voltage. In the finite displacement regime, larger mechanical loads increase the voltage and power density of the energy harvester. From the numerical experiments, it was revealed that significant enhancement in the electric voltage is obtained due to the increase in inhomogeneous mechanical strain suggesting the applications of nonlinear operating MEMS. However, the energy converting factor—when the structures undergo finite displacements—is quite small, so improving the performance of microstructure energy harvester is one of the future studies where some shape optimization or topology optimization methods can be applied to optimize the converting factor.

We also indicated that, at the micro-scale level, flexoelectricity is the dominant coupling effect over its piezoelectric counterpart. When decreasing the structural dimensions, the piezoelectric effect becomes less significant and the flexoelectric effect offers a larger contribution to the total electrical response.

Acknowledgements The authors would like to thank the financial support of ERC Starting Grant (802205) and Heisenberg-Programme from DFG (ZH 459/5-1). The authors would like to thank the financial support of RISE-BESTOFRAC (734379) of Horizon 2020.

Funding Open Access funding enabled and organized by Projekt DEAL. The authors have not disclosed any funding.

Data availability The data that support the findings of this study are available from the corresponding author upon reasonable request.

Declarations

Conflict of interest The authors declare that they have no known competing financial interests or personal relationships that could have appeared to influence the work reported in this paper.

Appendices

Appendix A. Couple stress-based flexoelectricity model

In couple stress theory, the third-order strain gradient $\epsilon_{ij,k}$ is replaced by a traceless second-order tensor $\kappa_{ij} = -e_{iab}\epsilon_{ja,b}$ [8,9]. The strain gradient tensor can be decomposed into a symmetric and an antisymmetric part as $\kappa_{ij} = \kappa^s_{ij} + \kappa^a_{ij}$. The antisymmetric tensor κ^a_{ij} can be represented by its corresponding dual vector $\chi_i = \frac{1}{2}e_{ijk}\kappa^a_{kj}$. The strain gradient elastic energy density is given by

$$\frac{1}{2}\epsilon_{ij,k}\tilde{H}_{ijklmn}\epsilon_{lm,n} = \frac{1}{2}\kappa^s_{ij}B_{ijkl}\kappa^s_{kl} + \frac{1}{2}\chi_i\tilde{B}_{ij}\chi_j \tag{A.1}$$

with

$$B_{ijkl} = g_1(\delta_{ik}\delta_{jl} + \delta_{il}\delta_{jk}) \quad \text{and} \quad \tilde{B}_{ij} = 16g_2\delta_{ij} \tag{A.2}$$

where g_1 and g_2 are two material parameters of the nonlocal elasticity, i.e., $g_1 = l_1^2 C_{12}$ and $g_2 = l_2^2 C_{12}$. By using κ_{ij} as the strain gradient metric, the flexoelectric tensor is $\tilde{f}_{ijk} = -e_{jab}f_{ikab}$. Denoting $\tilde{f} = \frac{\tilde{f}_{1122} - \tilde{f}_{1212}}{2}$, we have

$$\begin{aligned}\tilde{f}_{ijk}P_i\kappa_{jk} &= \tilde{f}_{ijk}P_i(\kappa^a_{jk} + \kappa^s_{jk}) \\ &= \tilde{f}_{ijk}P_i\kappa^a_{jk} = 2\tilde{f}P_i\chi_i\end{aligned} \tag{A.3}$$

This means the symmetric part of κ_{ij} does not contribute to the flexoelectric coupling effect. The internal energy density is rewritten as [48,49]

$$\psi(\epsilon_{ij}, \kappa^s_{ij}, \chi_i) = \psi^{int}(\epsilon_{ij}, \kappa^s_{ij}, \chi_i) + \frac{A_{ij}}{2}P_iP_j + 2\tilde{f}P_i\chi_i + d_{ijk}P_i\epsilon_{jk} \tag{A.4}$$

with

$$\psi^{int}(\epsilon_{ij}, \kappa^s_{ij}, \chi_i) = \frac{1}{2}\epsilon_{ij}\tilde{C}_{ijkl}\epsilon_{kl} + 8g_2\chi_i\chi_i + g_1\kappa^s_{ij}\kappa^s_{ij}. \tag{A.5}$$

The constitutive equations can be expressed as

$$\sigma_{ij} = \frac{\partial\psi}{\partial\epsilon_{ij}} = \tilde{C}_{ijkl}\epsilon_{kl} + d_{ijk}P_k,$$

$$s^s_{ij} = \frac{\partial\psi}{\partial\kappa^s_{ij}} = 2g_1\kappa^s_{ij},$$

$$s^a_i = \frac{\partial\psi}{\partial\chi_i} = 16g_2\chi_i + 2\tilde{f}P_i \text{ or } s^a_{ij}$$

$$= \frac{\partial \psi}{\partial \kappa_{ij}^a} = 8g_2\kappa_{ij}^a + \tilde{f}_{ijk}P_k \tag{A.6}$$

let's denote $\sigma_{ij}^m = \tilde{C}_{ijkl}\epsilon_{kl}$ and $s_i^m = 16g_2\chi_i$ or $s_{ij}^m = 8g_2\kappa_{ij}^a$. The governing equation and corresponding boundary conditions are obtained by applying the principle of energy balance.

Appendix B. IGA-based for spatial discretization

B-spline functions are computed from the Cox-de Boor recursion as

$$\tilde{N}_i^p(\xi) = \frac{\xi - \xi_i}{\xi_{i+p} - \xi_i}\tilde{N}_i^{p-1}(\xi) + \frac{\xi_{i+p+1} - \xi}{\xi_{i+p+1} - \xi_{i+1}}\tilde{N}_{i+1}^{p-1}(\xi), \tag{B.1}$$

with

$$\tilde{N}_i^0 = \begin{cases} 1, \text{ if } \xi_i \le \xi \le \xi_{i+1} \\ 0, \text{ otherwise.} \end{cases} \tag{B.2}$$

NURBS are defined as

$$N_i^p = \frac{\tilde{N}_i^p(\xi)w_i}{\sum_{i=0}^n \tilde{N}_i^p(\xi)w_i}. \tag{B.3}$$

The displacement $\mathbf{u}$ and its test function $\delta\mathbf{u}$ belong to the following spaces:

$$\begin{aligned} \mathcal{U} \in \{\mathbf{u} \in H^2(\Omega) | \mathbf{u} &= \mathbf{u}^* \text{ on } \Gamma_{u^*} \text{ and } \hat{\mathbf{N}} \cdot \nabla \mathbf{u} \\ &= \mathbf{u}^{**} \text{ on } \Gamma_{u^{**}}\}, \\ \mathcal{U}_0 \in \{\delta\mathbf{u} \in H^2(\Omega) | \delta\mathbf{u} &= \mathbf{0} \text{ on } \Gamma_{u^*} \text{ and } \hat{\mathbf{N}} \cdot \nabla \delta\mathbf{u} \\ &= \mathbf{0} \text{ on } \Gamma_{u^{**}}\}, \end{aligned} \tag{B.4}$$

where the interpolation of i^{th} nodal variables of the elements is used as $\mathbf{u} = \sum_i \mathbf{N}_u^i \cdot \tilde{\mathbf{u}}^i$, $\delta\mathbf{u} = \sum_i \mathbf{N}_u^i \cdot \delta\tilde{\mathbf{u}}^i$ and

$$\mathbf{u} = \begin{bmatrix} u_1 \\ u_2 \end{bmatrix}; \delta\mathbf{u} = \begin{bmatrix} \delta u_1 \\ \delta u_2 \end{bmatrix}; \mathbf{N}_u^i = \begin{bmatrix} N^i & 0 \\ 0 & N^i \end{bmatrix};$$
$$\tilde{\mathbf{u}}^i = \begin{bmatrix} \tilde{u}_1^i \\ \tilde{u}_2^i \end{bmatrix}; \delta\tilde{\mathbf{u}}^i = \begin{bmatrix} \delta\tilde{u}_1^i \\ \delta\tilde{u}_2^i \end{bmatrix}. \tag{B.5}$$

Similarly, the electric potentials is expressed as

$$\begin{aligned} &\Phi \in \{\phi \in H^1(\Omega) | \phi = \phi^* \text{ on } \Gamma_{\phi^*}\} \quad \text{and} \\ &\Phi_0 \in \{\delta\phi \in H^1(\Omega) | \delta\phi = 0 \text{ on } \Gamma_{\phi^*}\} \end{aligned} \tag{B.6}$$

where $\boldsymbol{\phi} = \sum_i \mathbf{N}_\phi^i \cdot \tilde{\boldsymbol{\phi}}^i$ and $\delta\boldsymbol{\phi} = \sum_i \mathbf{N}_\phi^i \cdot \delta\tilde{\boldsymbol{\phi}}^i$. Quadratic NURBS functions are adopted in this work. The strain tensor and its variation are computed, respectively, as

$$\boldsymbol{\epsilon} = \begin{bmatrix} \epsilon_{11} \\ \epsilon_{22} \\ 2\epsilon_{12} \end{bmatrix} = \begin{bmatrix} u_{1,1} + 0.5u_{k,1}u_{k,1} \\ u_{2,2} + 0.5u_{k,2}u_{k,2} \\ u_{1,2} + u_{2,1} + u_{k,1}u_{k,2} \end{bmatrix}, \tag{B.7}$$

$$\delta\boldsymbol{\epsilon} = \begin{bmatrix} \delta\epsilon_{11} \\ \delta\epsilon_{22} \\ 2\delta\epsilon_{12} \end{bmatrix} = \sum_i \begin{bmatrix} \frac{\partial N^i}{\partial X_1}(1 + u_{1,1}) & \frac{\partial N^i}{\partial X_1}u_{2,2} \\ \frac{\partial N^i}{\partial X_2}u_{2,1} & \frac{\partial N^i}{\partial X_2}(1 + u_{2,2}) \\ \frac{\partial N^i}{\partial X_2}(1 + u_{1,1}) + \frac{\partial N^i}{\partial X_1}u_{2,1} & +\frac{\partial N^i}{\partial X_1}(1 + u_{2,2}) + \frac{\partial N^i}{\partial X_2}u_{1,2} \end{bmatrix} \begin{bmatrix} \delta u_1 \\ \delta u_2 \end{bmatrix} \tag{B.8}$$

The nonzero component of 2D rotational tensor $\boldsymbol{\kappa}$ is

$$\begin{aligned} \kappa_{31} &= \frac{1}{2}(u_{2,11} - u_{1,12} + u_{k,11}u_{k,2} - u_{k,12}u_{k,1}) \\ \kappa_{32} &= \frac{1}{2}(u_{2,12} - u_{1,22} + u_{k,12}u_{k,2} - u_{k,22}u_{k,1}) \end{aligned} \tag{B.9}$$

The vector form of $\boldsymbol{\kappa}^s$ and $\boldsymbol{\kappa}^a$ are presented, respectively, as

$$\boldsymbol{\chi}^s = \begin{bmatrix} \frac{1}{2}\kappa_{32} \\ \frac{1}{2}\kappa_{31} \end{bmatrix} \text{ and } \boldsymbol{\chi}^a = \begin{bmatrix} \frac{1}{2}\kappa_{32} \\ -\frac{1}{2}\kappa_{31} \end{bmatrix} \tag{B.10}$$

and their corresponding variations are

$$\delta\boldsymbol{\chi}^s = \frac{1}{4}\begin{bmatrix} \frac{\partial^2 N^i}{\partial^2 X_2}(1 + u_{1,1}) + \frac{\partial^2 N^i}{\partial X_1 \partial X_2}u_{1,2} + \frac{\partial N^i}{\partial X_2}u_{1,12} - \frac{\partial N^i}{\partial X_1}u_{1,22} & \frac{\partial^2 N^i}{\partial X_1 \partial X_2}(1 + u_{2,2}) - \frac{\partial^2 N^i}{\partial X_2}u_{2,1} + \frac{\partial N^i}{\partial X_2}u_{2,12} - \frac{\partial N^i}{\partial X_1}u_{2,22} \\ -\frac{\partial^2 N^i}{\partial X_1 \partial X_2}(1 + u_{1,1}) + \frac{\partial^2 N^i}{\partial X_1^2}u_{1,2} + \frac{\partial N^i}{\partial X_2}u_{1,11} - \frac{\partial N^i}{\partial X_1}u_{1,12} & \frac{\partial^2 N^i}{\partial^2 X_1}(1 + u_{2,2}) - \frac{\partial^2 N^i}{\partial X_1 \partial X_2}u_{2,1} + \frac{\partial N^i}{\partial X_2}u_{2,11} - \frac{\partial N^i}{\partial X_1}u_{2,12} \end{bmatrix} \cdot \begin{bmatrix} \delta u_1 \\ \delta u_2 \end{bmatrix} \tag{B.11}$$

$$\delta\boldsymbol{\chi}^a = \frac{1}{4}\begin{bmatrix} \frac{\partial^2 N^i}{\partial^2 X_2}(1 + u_{1,1}) + \frac{\partial^2 N^i}{\partial X_1 \partial X_2}u_{1,2} + \frac{\partial N^i}{\partial X_2}u_{1,12} - \frac{\partial N^i}{\partial X_1}u_{1,22} & \frac{\partial^2 N^i}{\partial X_1 \partial X_2}(1 + u_{2,2}) - \frac{\partial^2 N^i}{\partial X_2}u_{2,1} + \frac{\partial N^i}{\partial X_2}u_{2,12} - \frac{\partial N^i}{\partial X_1}u_{2,22} \\ \frac{\partial^2 N^i}{\partial X_1 \partial X_2}(1 + u_{1,1}) - \frac{\partial^2 N^i}{\partial X_1^2}u_{1,2} - \frac{\partial N^i}{\partial X_2}u_{1,11} + \frac{\partial N^i}{\partial X_1}u_{1,12} & -\frac{\partial^2 N^i}{\partial^2 X_1}(1 + u_{2,2}) + \frac{\partial^2 N^i}{\partial X_1 \partial X_2}u_{2,1} - \frac{\partial N^i}{\partial X_2}u_{2,11} + \frac{\partial N^i}{\partial X_1}u_{2,12} \end{bmatrix} \cdot \begin{bmatrix} \delta u_1 \\ \delta u_2 \end{bmatrix} \tag{B.12}$$

Appendix C: Expressions of equation of motion for linear frequency response

The components of equation (27) are computed as (the dynamic of polarization is neglected, i.e., $\gamma_{ij} = 0$)

$$
\begin{aligned}
\delta u_i \bar{K}^{ij}_{uu} u_j &= \int_\Omega \Big(\sigma^m_{ij}\epsilon_{ij} + s^m_i \delta\chi_i + s^s_{ij}\delta\kappa_{ij} \\
&\quad - A^{-1}_{im}(2\tilde{f}\chi_i + d_{ijk}\epsilon_{jk})(2\tilde{f}\delta\chi_m + d_{mjk}\delta\epsilon_{jk})\Big)d\Omega, \\
\delta u_i \bar{\bar{K}}^{ij}_{uu} \ddot{u}_j &= -A^{-1}_{im}\int_\Omega (2\tilde{f}\ddot{\chi}_i + d_{ijk}\ddot{\epsilon}_{jk})m_{mk}\delta u_k d\Omega \\
&\quad - A^{-1}_{im}\int_\Omega (2\tilde{f}\chi_i + d_{ijk}\epsilon_{jk})m_{mk}\delta\ddot{u}_k d\Omega, \\
\delta u_i \bar{\bar{K}}^{ij}_{uu} \ddot{\ddot{u}}_j &= -A^{-1}_{im}\int_\Omega m_{ij}\ddot{\ddot{u}}_j m_{mk}\delta u_k d\Omega, \\
\delta u_i \bar{K}^{ij}_{u\phi}\phi_j &= -A^{-1}_{im}\int_\Omega \phi_{,m}(2\tilde{f}\delta\chi_i + d_{ijk}\delta\epsilon_{jk})d\Omega, \\
\delta u_i \bar{\bar{K}}^{ij}_{u\phi}\ddot{\phi}_j &= -A^{-1}_{im}\int_\Omega \ddot{\phi}_{,m} m_{ij}\delta u_j d\Omega, \\
D^{ij} &= \alpha_1 M^{ij} + \alpha_2 \bar{K}^{ij}_{uu}
\end{aligned}
\tag{C.1}
$$

References

1. Nix, W.D.: Mechanical properties of thin films. Metall. Trans. A **20**(11), 2217 (1989)
2. Fleck, N., Muller, G., Ashby, M.F., Hutchinson, J.W.: Strain gradient plasticity: theory and experiment. Acta Metall. Mater. **42**(2), 475–487 (1994)
3. Stölken, J.S., Evans, A.: A microbend test method for measuring the plasticity length scale. Acta Mater. **46**(14), 5109–5115 (1998)
4. Jing, G., Duan, H., Sun, X., Zhang, Z., Xu, J., Li, Y., Wang, J., Yu, D.: Surface effects on elastic properties of silver nanowires: contact atomic-force microscopy. Phys. Rev. B **73**(23), 235409 (2006)
5. Lam, D.C., Yang, F., Chong, A., Wang, J., Tong, P.: Experiments and theory in strain gradient elasticity. J. Mech. Phys. Solids **51**(8), 1477–1508 (2003)
6. Liebold, C., Müller, W.H.: Comparison of gradient elasticity models for the bending of micromaterials. Comput. Mater. Sci. **116**, 52–61 (2016)
7. Okabe, T., Takeda, N.: Size effect on tensile strength of unidirectional CFRP composites-experiment and simulation. Compos. Sci. Technol. **62**(15), 2053–2064 (2002)
8. Mindlin, R., Tiersten, H.: Effects of couple-stresses in linear elasticity. Arch. Ration. Mech. Anal. **11**, 415–448 (1962)
9. Toupin, R.A.: Elastic materials with couple-stresses. Arch. Ration. Mech. Anal. **11**(1), 385–414 (1962)
10. Koiter, W.T.: Couple stresses in the theory of elasticity. Proc. K. Ned. Akad. Wet. B **67**, 17–44 (1964)
11. Mindlin, R.D.: Microstructure in linear elasticity. Arch. Ration. Mech. Anal. **16**, 51–78 (1964)
12. Eringen, A.C., Suhubi, E.: Nonlinear theory of simple micro-elastic solids I. Int. J. Eng. Sci. **2**(2), 189–203 (1964)
13. Green, A.E., Rivlin, R.S.: Multipolar continuum mechanics. Arch. Ration. Mech. Anal. **17**(2), 113–147 (1964)
14. Kröner, E.: Elasticity theory of materials with long range cohesive forces. Int. J. Solids Struct. **3**(5), 731–742 (1967)
15. Mindlin, R.D., Eshel, N.N.: On first strain-gradient theories in linear elasticity. Int. J. Solids Struct. **4**(1), 109–124 (1968)
16. Germain, P.: The method of virtual power in continuum mechanics. Part 2: microstructure. SIAM J. Appl. Math. **25**(3), 556–575 (1973)
17. Mindlin, R.D.: Second gradient of strain and surface-tension in linear elasticity. Int. J. Solids Struct. **1**(4), 417–438 (1965)
18. Gurtin, M.E., Murdoch, A.I.: A continuum theory of elastic material surfaces. Arch. Ration. Mech. Anal. **57**(4), 291–323 (1975)
19. Gurtin, M.E., Murdoch, A.I.: Surface stress in solids. Int. J. Solids Struct. **14**(6), 431–440 (1978)
20. Eringen, A.C.: On differential equations of nonlocal elasticity and solutions of screw dislocation and surface waves. J. Appl. Phys. **54**(9), 4703–4710 (1983)
21. Multani, M., Gokarn, S., Palkar, V., Vijayaraghavan, R.: Morphotropic phase boundary in the system pb (zrxti1-x) o3. Mater. Res. Bull. **17**(1), 101–104 (1982)
22. Mishima, T., Fujioka, H., Nagakari, S., Kamigaki, K., Nambu, S.: Lattice image observations of nanoscale ordered regions in pb (mg1/3nb2/3) o3. Jpn. J. Appl. Phys. **36**(9S), 6141 (1997)
23. Buhlmann, S., Dwir, B., Baborowski, J., Muralt, P.: Size effect in mesoscopic epitaxial ferroelectric structures: increase of piezoelectric response with decreasing feature size. Appl. Phys. Lett. 80, 3195–3197 (2002)
24. Cross, L.E.: Flexoelectric effects: charge separation in insulating solids subjected to elastic strain gradients. J. Mater. Sci. **41**(1), 53–63 (2006)
25. Harden, J., Mbanga, B., Éber, N., Fodor-Csorba, K., Sprunt, S., Gleeson, J.T., Jakli, A.: Giant flexoelectricity of bent-core nematic liquid crystals. Phys. Rev. Lett. **97**(15), 157802 (2006)
26. Baskaran, S., He, X., Chen, Q., Fu, J.Y.: Experimental studies on the direct flexoelectric effect in α-phase polyvinylidene fluoride films. Appl. Phys. Lett. **98**(24), 242901 (2011)
27. Catalan, G., Lubk, A., Vlooswijk, A., Snoeck, E., Magen, C., Janssens, A., Rispens, G., Rijnders, G., Blank, D.H., Noheda, B.: Flexoelectric rotation of polarization in ferroelectric thin films. Nat. Mater. **10**(12), 963–967 (2011)
28. Jiang, X., Huang, W., Zhang, S.: Flexoelectric nano-generator: materials, structures and devices. Nano Energy **2**(6), 1079–1092 (2013)
29. Bhaskar, U.K., Banerjee, N., Abdollahi, A., Wang, Z., Schlom, D.G., Rijnders, G., Catalan, G.: A flexoelectric microelectromechanical system on silicon. Nat. Nanotechnol. **11**(3), 263–266 (2016)
30. Rey, A. D., Servio, P., Herrera Valencia, E. E.: Stress-sensor device based on flexoelectric liquid crystalline membranes. ChemPhysChem **15**(7), 1405–1412 (2014)
31. Wei, C., Wang, Z., Huang, W.: Performance of a flexoelectric actuator for lamb wave excitation. J. Appl. Phys. **129**(3), 034902 (2021)
32. Deng, Q., Kammoun, M., Erturk, A., Sharma, P.: Nanoscale flexoelectric energy harvesting. Int. J. Solids Struct. **51**(18), 3218–3225 (2014)
33. Faroughi, S., Rojas, E., Abdelkefi, A., Park, Y.: Reduced-order modeling and usefulness of non-uniform beams for

flexoelectric energy harvesting applications. Acta Mech. **230**(7), 2339–2361 (2019)
34. Deng, Q., Shen, S.: The flexodynamic effect on nanoscale flexoelectric energy harvesting: a computational approach. Smart Mater. Struct. **27**(10), 105001 (2018)
35. Wang, K., Wang, B.: Non-linear flexoelectricity in energy harvesting. Int. J. Eng. Sci. **116**, 88–103 (2017)
36. Raj, P.R., Santhosh, B.: Parametric study and optimization of linear and nonlinear vibration absorbers combined with piezoelectric energy harvester. Int. J. Mech. Sci. **152**, 268–279 (2019)
37. Caetano, V.J., Savi, M.A.: Star-shaped piezoelectric mechanical energy harvesters for multidirectional sources. Int. J. Mech. Sci. **215**, 106962 (2022)
38. Chu, L., Li, Y., Dui, G.: Nonlinear analysis of functionally graded flexoelectric nanoscale energy harvesters. Int. J. Mech. Sci. **167**, 105282 (2020)
39. Majdoub, M., Sharma, P., Cagin, T.: Enhanced size-dependent piezoelectricity and elasticity in nanostructures due to the flexoelectric effect. Phys. Rev. B **77**(12), 125424 (2008)
40. Moura, A.G., Erturk, A.: Electroelastodynamics of flexoelectric energy conversion and harvesting in elastic dielectrics. J. Appl. Phys. **121**(6), 064110 (2017)
41. Metrikine, A., Askes, H.: An isotropic dynamically consistent gradient elasticity model derived from a 2d lattice. Philos. Mag. **86**(21–22), 3259–3286 (2006)
42. Askes, H., Metrikine, A.V.: One-dimensional dynamically consistent gradient elasticity models derived from a discrete microstructure: Part 2: static and dynamic response. Euro. J. Mech.-A/Solids **21**(4), 573–588 (2002)
43. Askes, H., Aifantis, E.C.: Gradient elasticity in statics and dynamics: an overview of formulations, length scale identification procedures, finite element implementations and new results. Int. J. Solids Struct. **48**(13), 1962–1990 (2011)
44. Tagantsev, A.: Theory of flexoelectric effect in crystals. Zh. Eksp. Teor. Fiz. **88**(6), 2108–22 (1985)
45. Harris, P.: Mechanism for the shock polarization of dielectrics. J. Appl. Phys. **36**(3), 739–741 (1965)
46. Yudin, P., Tagantsev, A.: Fundamentals of flexoelectricity in solids. Nanotechnology **24**(43), 432001 (2013)
47. Thai, T.Q., Zhuang, X., Park, H.S., Rabczuk, T.: A staggered explicit-implicit isogeometric formulation for large deformation flexoelectricity. Eng. Anal. Bound. Elem. **122**, 1–12 (2021)
48. Anqing, L., Shenjie, Z., Lu, Q., Xi, C.: A flexoelectric theory with rotation gradient effects for elastic dielectrics. Modell. Simul. Mater. Sci. Eng. **24**(1), 015009 (2015)
49. Poya, R., Gil, A.J., Ortigosa, R., Palma, R.: On a family of numerical models for couple stress based flexoelectricity for continua and beams. J. Mech. Phys. Solids **125**, 613–652 (2019)
50. Mao, S., Purohit, P.K.: Insights into flexoelectric solids from strain-gradient elasticity. J. Appl. Mech. **81**(8), 081004 (2014)
51. Hong, J., Vanderbilt, D.: First-principles theory and calculation of flexoelectricity. Phys. Rev. B **88**(17), 174107 (2013)
52. Kvasov, A., Tagantsev, A.K.: Dynamic flexoelectric effect in perovskites from first-principles calculations. Phys. Rev. B **92**(5), 054104 (2015)
53. Hughes, T.J.: The Finite Element Method: Linear Static and Dynamic Finite Element Analysis. Courier Corporation (2012)
54. Belytschko, T., Liu, W.K., Moran, B., Elkhodary, K.: Nonlinear Finite Elements for Continua and Structures. Wiley (2013)
55. Roh, Y., Varadan, V.V., Varadan, V.K.: Characterization of all the elastic, dielectric, and piezoelectric constants of uniaxially oriented poled PVDF films. IEEE Trans. Ultrason. Ferroelectr. Freq. Control **49**(6), 836–847 (2002)
56. Chu, B., Salem, D.: Flexoelectricity in several thermoplastic and thermosetting polymers. Appl. Phys. Lett. **101**(10), 103905 (2012)
57. Bell, R., Rupprecht, G.: Elastic constants of strontium titanate. Phys. Rev. **129**(1), 90 (1963)
58. Sawaguchi, E., Kikuchi, A., et al.: Dielectric constant of strontium titanate at low temperatures. J. Phys. Soc. Jpn. **17**(10), 1666–1667 (1962)
59. Sun, F., Khassaf, H., Alpay, S.: Strain engineering of piezoelectric properties of strontium titanate thin films. J. Mater. Sci. **49**(17), 5978–5985 (2014)
60. Shu, L., Liang, R., Rao, Z., Fei, L., Ke, S., Wang, Y.: Flexoelectric materials and their related applications: a focused review. J. Adv. Ceram. **8**(2), 153–173 (2019)
61. Frantziskonis, G., Aifantis, E.C.: On the stochastic interpretation of gradient-dependent constitutive equations. Eur. J. Mech.-A/Solids **21**(4), 589–596 (2002)
62. Aifantis, E.C.: Update on a class of gradient theories. Mech. Mater. **35**(3–6), 259–280 (2003)
63. Askes, H., Wang, B., Bennett, T.: Element size and time step selection procedures for the numerical analysis of elasticity with higher-order inertia. J. Sound Vibr. **314**(3–5), 650–656 (2008)
64. Shenck, N.S., Paradiso, J.A.: Energy scavenging with shoe-mounted piezoelectrics. IEEE Micro **21**(3), 30–42 (2001)
65. Cavagna, G., Mantovani, M., Willems, P., Musch, G.: The resonant step frequency in human running. Pflugers Arch. **434**(6), 678–684 (1997)
66. Thai, T.Q., Zhuang, X., Rabczuk, T.: A nonlinear geometric couple stress based strain gradient Kirchhoff-love shell formulation for microscale thin-wall structures. Int. J. Mech. Sci. **196**, 106272 (2021)